POLITECNICO DI TORINO

Collegio di Ingegneria Energetica

**Corso di Laurea Magistrale**
**in Ingegneria Energetica E Nucleare**

Tesi di Laurea Magistrale

# Modelling of a new CSP dish system with PCM storage in a Modelica environment


**Relatore**

prof. Eliodoro Chiavazzo

**Candidato**

Vincenzo Piras


Aprile 2018

**Abstract**

The highest solar to electricity efficiency ever registered for CSP technologies has been obtained using a Dish Stirling System. The lack of a proper dispatchability, however, has overshadowed this technology with respect to the other CSP systems, making it compete directly with the cheaper PV. The integration of a storage system could play a very important role in its evolution.

The aim of this thesis work is the evaluation of the economic feasibility of a new Dish Stirling concept coupled with a PCM storage developed by the company Cleanergy.

Two different Modelica models of the storage have been developed and the effect of the PCM block aspect ratio on the system efficiency has been studied. The economic analysis based on the developed models shows promising results (LCOE around 75€/MWh and IRR around 5.5% for the Woomera case study) that are highly dependent on the location selection and on the adopted tariff scheme.

# Contents

# List of Figures

# List of Tables



# List of Symbols

| | |
|---|---|
| $A$ | Area $[m^2]$ |
| $G_{sc}$ | Solar Constant $[W/m^2]$ |
| $P$ | Power $[W]$ |
| $Q$ | Energy $[J]$ |
| $T$ | Temperature $[K]$ |
| $V$ | Volume $[m^3]$ |
| $\rho$ | Density $[kg/m^3]$ |
| $\Phi$ | Thermal Power $[W]$ |
| $h$ | Specitif Enthalpy $[J/kg]$ |
| $h_{conv}$ | Convection Heat Transfer Coefficient $[W/(m^2K)]$ |

# List of Abbreviations

**AUD** Australian Dollar

**BOP** Balance of Plant

**CF** Capacity Factor

**CR** Concentration ratio

**CSP** Concentrated solar power

**DCS** Dispatch Control Strategy

**IRR** Internal Rate of Return

**LCOE** Levelized cost of electricity

**LGC** Large Scale Generation Certificate

**PC** Phase Change

**PCM** Phase Change Material

**SM** Solar Multiple

**SOC** State Of Charge

**TES** Thermal Energy Storage

# 1 Introduction

The global energy systems are currently undergoing substantial changes as a consequence of the increasing interest in environmental issues and the use of renewable energy sources is increasing worldwide. Among the various technologies, one of the most promising in terms of energy potential are the solar energy technologies.
A key issue related to this source is the availability: in order to achieve a higher penetration into the grid, solar power should be available whenever energy is required, even if in that particular moment the sun is not shining.

Trough the use of a proper energy storage systems the dispatchability of those plants can be increased. The main alternatives when it comes to electricity production are two: use a PV plant coupled with a battery storage or use a Concentrated Solar Power Plant (CSP) coupled with a thermal energy storage.

This second alternative will be analysed considering a new CSP system developed by the Swedish company Cleanergy A.B. that will couple a PCM based storage with a solar dish Stirling system.

## 1.1 Thesis Objectives and Methodology

The main objective of the master thesis is the evaluation of the economical feasibility of the new solar dish Stirling concept developed by Cleanergy AB.
Two different storage models will be developed to study the PCM storage behaviour, together with a new operational strategy that will try to optimize the revenues obtainable from the system.

The analysis will be carried out according to the various steps presented below.

1. Theoretical Framework: a overview of the solar energy will be carried out underlining the huge amount of power that can be obtained from this source with respect to the other ones. An overview of the CSP systems, with particular interest in the solar dish, will be presented, together with the classification of the storage systems and the numerical method that are currently used to simulate phase change materials;

2. Presentation of the system: a very concise presentation of the storage concept used will be done, together with the presentation of the material properties that will be used during the study;

3. First 0D model: a simplified 0D model of the storage system will be developed and some comparison between the results for different aspect ration will be drawn.

4. FDM 1D model: a more complex FDM 1D model will be developed to describe the storage system. Some comparison with the two different developed models will be done.

5. Dispatch Strategy: A dispatch strategy for the analysed system will be developed to decide whenever to produce or not during the year. Some suitable performance indicators will be presented to check how the operational strategy is behaving.

6. Thermo-Economic Analysis - Boundary Conditions: the choice of a proper location for the system will be discussed together with the presentation of the tariff scheme considered in the study. The possibility of considering incentives in the study will be analysed. All the costs related to the CAPEX and OPEX evaluation and the methodology used in the calculation of the LCOE and the IRR of the system will be shown.

7. Results and Discussion: The results of the Thermo-Economic Analysis will be shown together with a sensitive analysis on the price variation and presence of incentives.

8. Conclusions: a final discussion on the results obtained will be done.

9. Model Limitations and Suggestions for future work: the model limitations and how future works could improve the model will be presented.

# 2 Theoretical Framework

## 2.1 Solar Energy Overview

The Sun is a natural fusion reactor in whose core hydrogen is fused to create helium. During this process a large amount of power is released from the sun to the outer space (around 4 million billion GW), but only a small portion of it reaches the earth.

The power from the sun received on a unit area of surface perpendicular to the direction of propagation of the radiation at mean earth-sun distance outside the atmosphere is called Solar Constant ($G_{sc}$) and has a value of 1367 $W/m^2$ [23]. This amount of power leads to an enormous quantity of energy coming from the sun every year, much larger than any other usable source. It's around 1500 times larger than the total world energy use (as shown in figure 1).

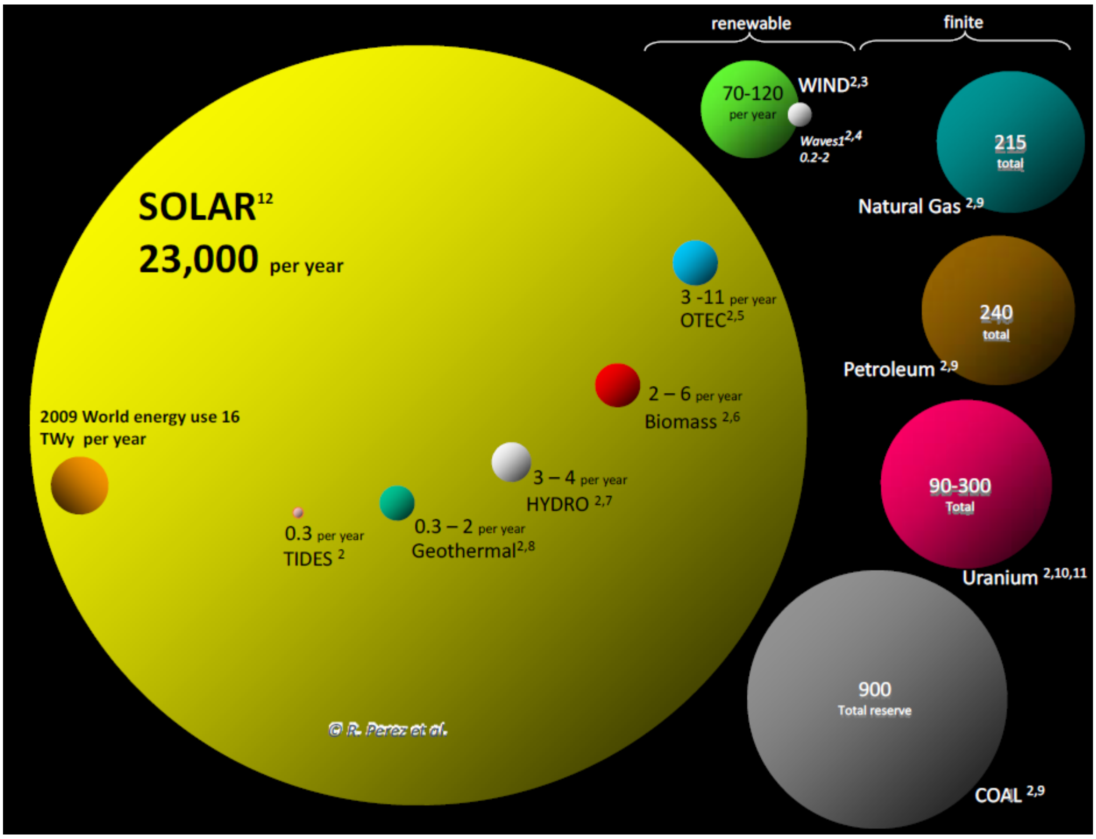


Figure 1: 2009 Estimate of finite and renewable planetary energy reserves (Terawatt-years). Total recoverable reserves are shown for the finite resources. Yearly potential is shown for the renewables. [28]

Even though its potential is very big, nowadays the sun provides only around 1% of all electricity used globally with his 227 $GW_e$ of global installed capacity in 2015 [49] and only 4.94 $GW_e$ comes from CSP power plants [20].

As it can be seen in figures 2 and 3 the trend of the installed capacity in both PV and CSP technology is positive and it is expected to increase in the successive years.

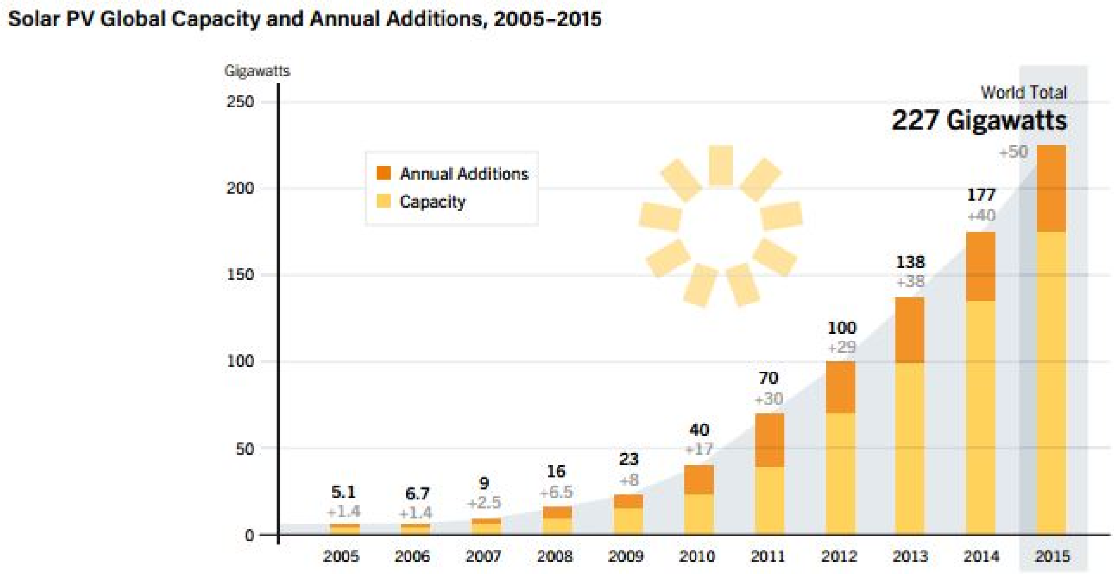


Figure 2: PV installed capacity growth [45]

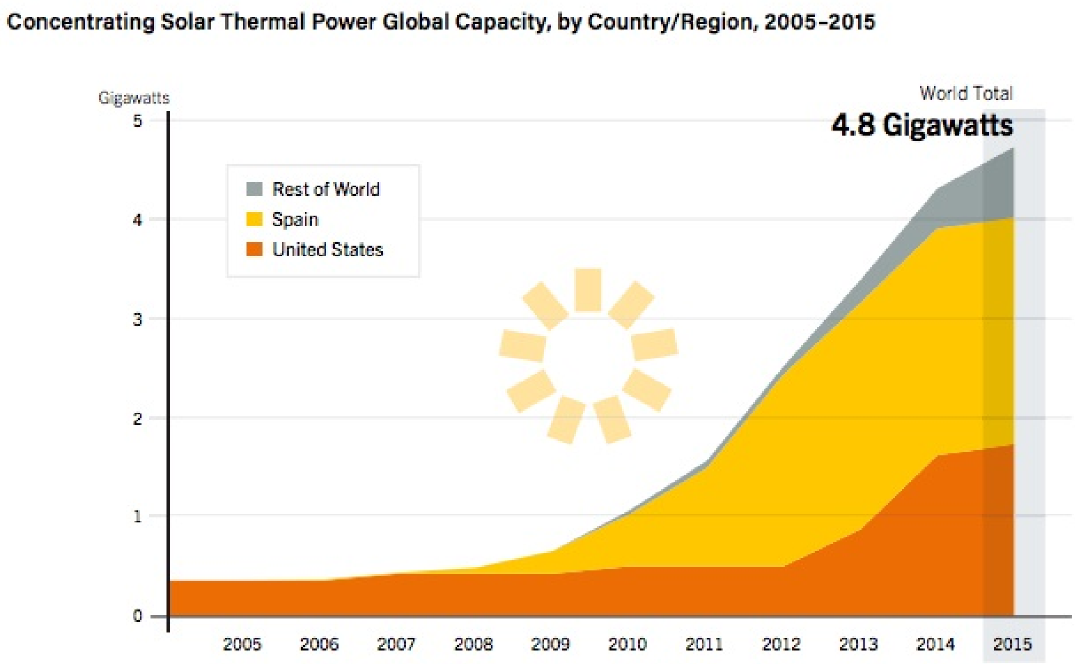


Figure 3: CSP installed capacity growth [45]

## 2.2 CSP technologies

CSP plants are solar thermal systems in which solar radiation is concentrated through the help of concentrators into a focal spot where the receiver is placed. The heat gained in it is than used as the heat source for a power conversion system. Finally the mechanical energy is converted into electricity by a generator. The schematic of this functioning is shown in figure 4. Storage and back up systems can be added to this basic schematic. A tracking system is usually embedded within the concentrator in order to make it follow the path of the sun maximizing the solar radiation gained by the receiver. It can be either a one-axis tracking system or two-axis tracking system.

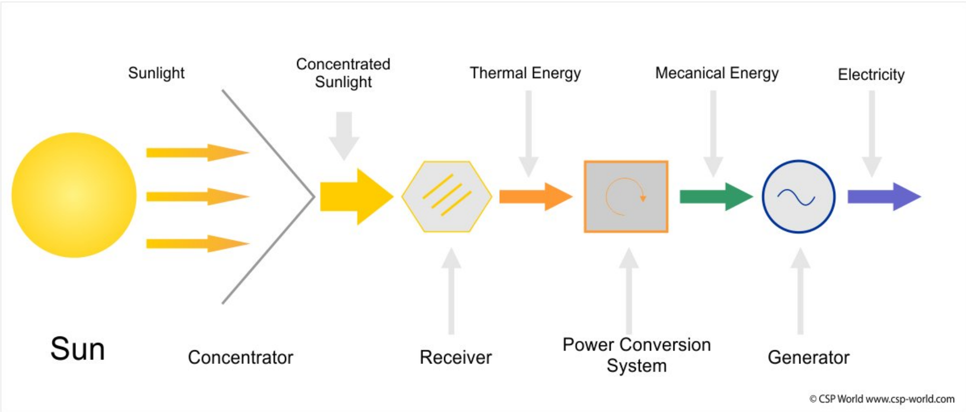


Figure 4: CSP schematic [11]

A very important parameter when it comes to evaluate the specific technology is the so called Concentration Ratio (CR). It is defined as the ratio between the intensity of the radiation before the concentration and the one in the focal spot after the concentration [47]. Higher is the concentration ratio, higher is the temperature which can be reached in the receiver and, so, the maximum possible achievable efficiency of the power conversion system.

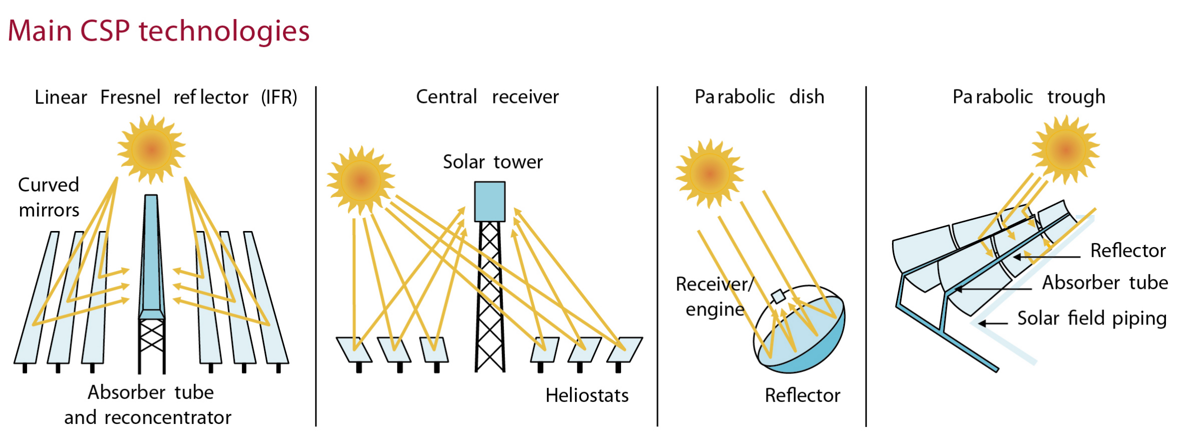


Figure 5: CSP technologies [29]

The CSP systems can be classified into 4 main categories shown in figure 5: Linear Fresnel Reflector (LFR), Parabolic Trough, Central Receiver and Parabolic Dish.

Linear Fresnel reflector and Parabolic Trough are linear concentration system while Central Receiver and Parabolic Dish are point concentration system. It mean that those last two can reach a higher CR with respect to the previous technologies [47].
In table 1 their characteristic are shown.

| Parameter | Concentration Ratio | Tracking system | Temperatures |
|---|---|---|---|
| Linear Fresnel | 15-60 | One-Axis | $\approx 500°C$ |
| Parabolic Trough | 30-100 | One-Axis | $\approx 600°C$ |
| Tower | 500-1'000 | Two Axis | $\approx 800°C$ |
| Parabolic Dish | 1'000-10'000 | Two Axis | $\approx 1400°C$ |

Table 1: Steam cycle parameters

### 2.2.1 Solar multiple and Capacity Factor

The Capacity Factor (CF) is a parameter that is generally used in every type of power plants to indicate how much energy a system produce with respect to its nominal power. It is defined as the ratio of the net electricity generated($E_{el,gen}$), for the time considered, to the energy that could have been generated at continuous full-power operation during the same period [34].

$$CF = \frac{E_{el,gen}}{P_{el,nom} * t} \tag{1}$$

Where $P_{el,nom}$ is the nominal electric power of the power block and t is the time interval considered. Usually this factor is refereed to the operation of the system during one year (t=8760h).

If a CSP system is design to match at the best design condition (maximum energy gained from the sun) the nominal power of the power block, the CF of the system will be very low. It would mean that the system is working as its nominal power for a very small amount of time. To avoid this issue the concentrator are often design to reflect into the receiver in the design condition more power with respect to the one required to run the system at nominal power.
This concept can be explained with the use of the solar multiple (SM). It is the ratio of the solar field design point thermal power output $Q_{des,field}$ (normally calculated at solar noon on a clear midsummer day) to the thermal power demand of the power block when running at its nominal capacity $Q_{des,PB}$ [25].

$$SM = \frac{Q_{des,field}}{Q_{des,PB}} \tag{2}$$

A visual representation of the solar multiple can be seen in figure 6.

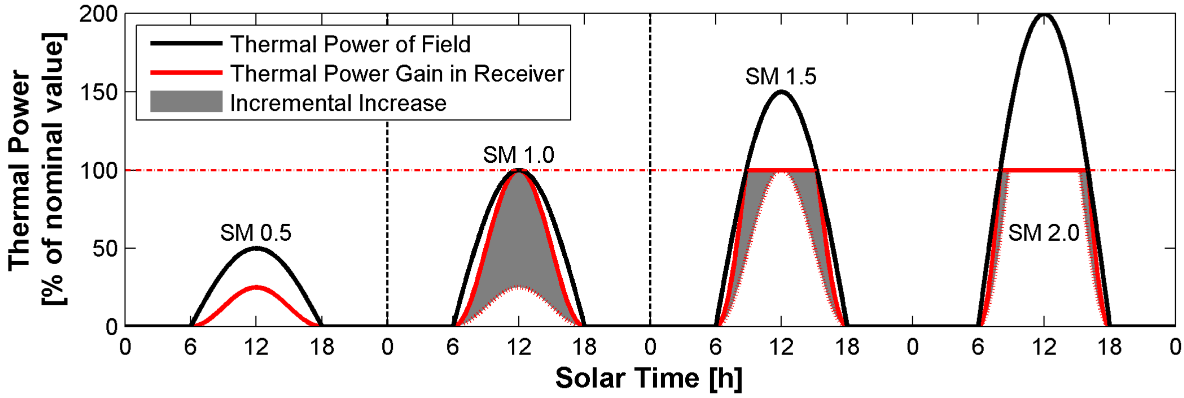


Figure 6: Solar Multiple [37]

If the system has no storage the SM is usually around 1.1 and 1.4 [25].

#### 2.2.2 Storage and Load configurations in CSP power plants

One of the key advantage of this technology, when compared to other renewable systems, is the possibility to integrate a cost efficient local storage system, increasing the dispatchability of the plants. The introduction of a thermal storage allows the uncoupling between the availability of the source and the production of electricity. The SM of the plant can also be increased as long as the surplus of energy that can be generated is no more wasted, but stored for a later use.

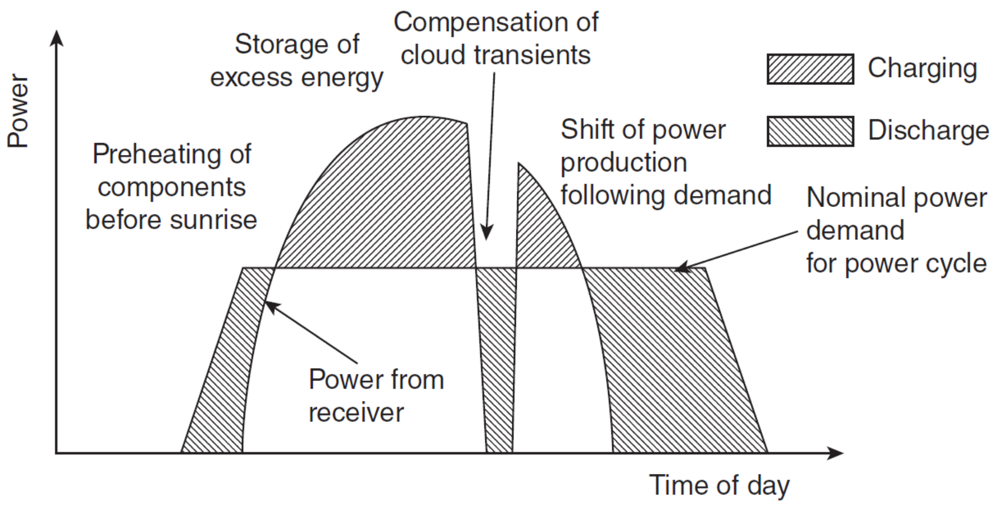


Figure 7: Storage Functioning [25]

The accumulated heat can be used at the beginning of the day to warm up the various components to guarantee a faster start-up, and during the day to either cover transients due to clouds or produce when the sun has set (figure 7).
Various strategies can be developed according to the desired type of production.

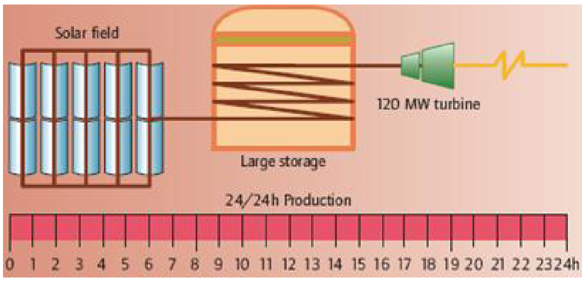


Figure 8: Base Load Configuration [35]

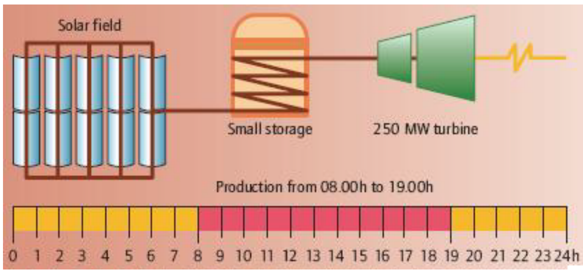


Figure 9: Intermediate load configuration [35]

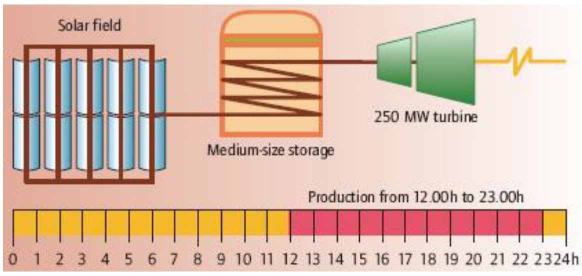


Figure 10: Delayed Intermediate Load Configuration [35]

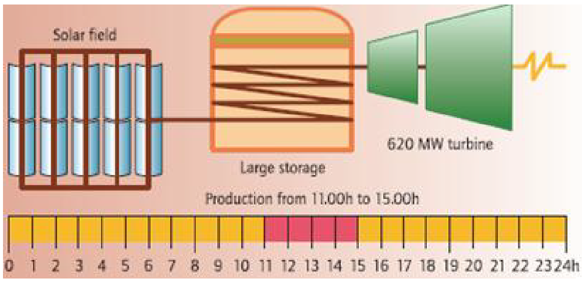


Figure 11: Peak load configuration [35]

In figures 8, 9, 10 and 8 four different strategies are shown. In case of a 24 hours production, a very large storage is needed since it should be able to store an amount of energy equal to the energy needed to run the system for more than half a day. In case of Intermediate load configuration, the storage needed is relatively small, considering that it is used to guarantee a stable production during the day. In case of a delayed intermediate load, the storage should be slightly larger because it must store the heat gained during the first half of the day. A very large storage is needed in case of a peak load configuration since it stores all the heat produced during the day and uses it during the peak energy demand.

In real cases the design is a more complex process that does not only involve the type of desired production, but also energy price fluctuation during the day, availability of sources, cost of the various component of the plant, complex storage strategies studied to maximize the profit obtainable from the plant.

## 2.3 CSP Parabolic Dish system

Among the various CSP technologies, the focus of this work will be on the Parabolic Dish Technology. A dish system consists of a parabolic shape concentrator, a tracking system, a solar heat exchanger (Receiver), an engine with generator and a system control unit (figure 12) [25].

The aim of the concentrators is to collect and direct the sun beam into a focal spot with an intensity much larger than than one hitting them [30].
The size of this component is determined by the power output desired at maximum insulation levels. In the concentrators, reflective surface of aluminum or silver in the back

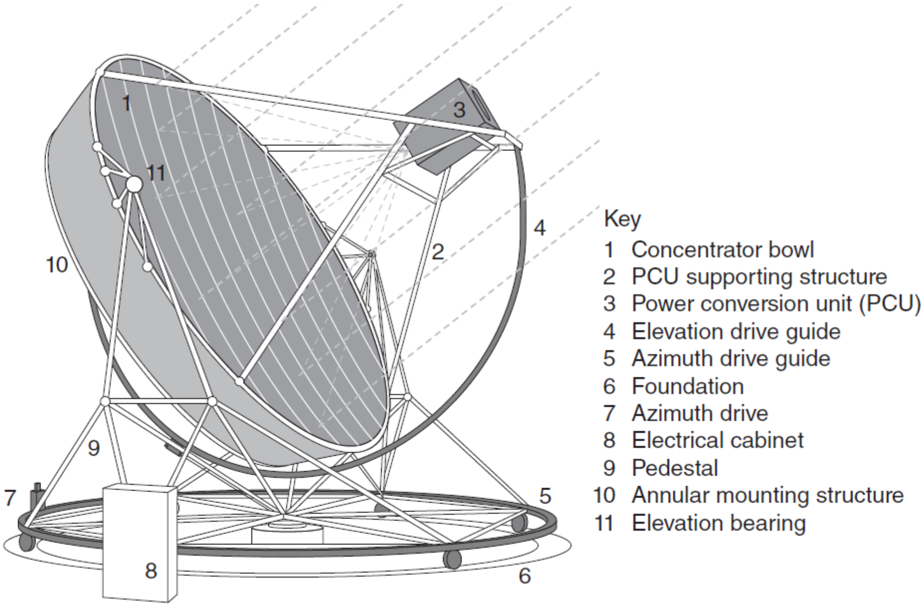


Figure 12: Schematic representation of an example of a dish system [25]

surface of glass or plastic are used.

### 2.3.1 Concentrators

Concentrators represent about 25% of the total cost of a Parabolic dish system. They are typically constructed using multiple glass facets mounted on a single frame, even if there are some attempts of forming full paraboloids from sheer metal with stretched membrane. [48] The concentrators can be classified in three main categories.

#### 2.3.1.1 Glass-Faceted concentrators

They use spherical curved glass mirror facets mounted on parabolic shaped structures. The small curvature of the mirrors makes easy to reach a high accuracy that guarantees a high concentration ratio. Those concentrators tend to be heavy end expensive and require accurate alignment of every single mirror. An example of such a configuration is the California Edison 25 kW dish/Stirling system shown in figure 13.

#### 2.3.1.2 Full-Surface Paraboloid Concentrators

They use mirrors which entire surface form a paraboloid. Example of this technology are the General Electric PDC-1 and the Acurex 15-m dish concentrator.

#### 2.3.1.3 Stretched-Membrane Concentrators

In this case, a thin membrane of a reflective plastic sheeting or a thin metal sheeting with a reflecting coating, stretched over both sides of a metal ring have been developed. A slight vacuum is create between the two membranes to obtain a concave shape.
The vacuum is not able to guarantee a proper paraboloid shape in case of a small ratio

Figure 13: California Edison 25 kW dish/Stirling system [38]

f/d (focal length over diameter) so a pre-shaping of the membraned can be obtained acting beyond its elastic limit. Another alternative is the use of a large number of small stretched-membrane facets mounted on a support frame. In this case less curvature is required and pre-shaping can be avoided (Multifaceted). In figures 14 and 15 examples of the two different type can be seen (respectively Single-faced and Multifaceted Stretched-Membrane concentrators).

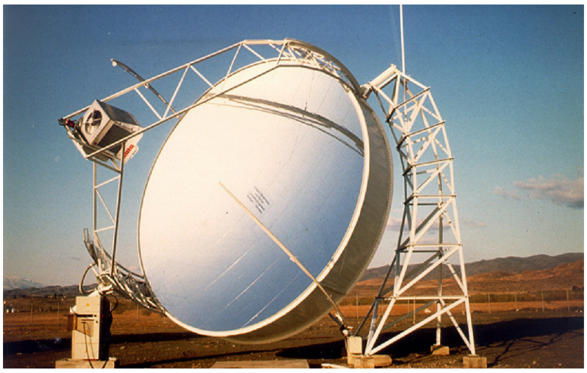

Figure 14: Schlaich Bergermann single membrane solar dish [36]

Figure 15: Dish/Stirling-engine system at Ft. Huachuca, Arizona, USA [12]

### 2.3.2 Tracking system

Two different types of tracking system can be used to make the concentrators face directly the sun (figure 16): azimuth-elevation tracking (a) and polar equatorial mounted system (b).

In the case of a azimuth-elevation tracking, the dish rotates in a plane parallel to the earth surface (azimuth) and around an axis perpendicular to it (elevation). The problem with this configuration is that the rotation rates in both the directions vary during the

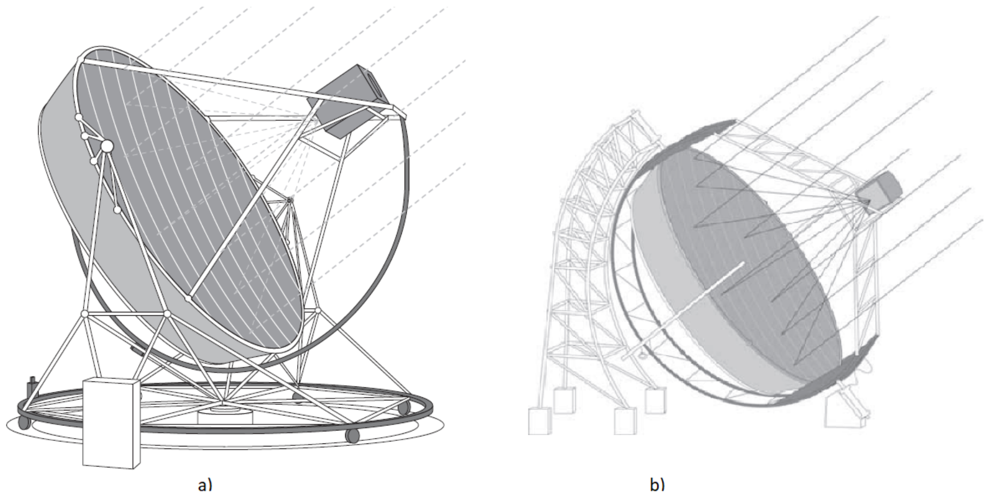


Figure 16: Schematic representation of the tracking systems [25]

day [25].
In the case of a polar-equatorial tracking method, the collector rotates around an axis parallel to the earth axis of rotation and an axis (declination axis) perpendicular to the polar axis. The first rotation in this case has a constant rotation rate of $15°/hour$ while the other feature a very slow rotation that varies by $\pm 23.5°$ [25].
Those mechanism are normally driven by electrical motors and the tracking position is found either with sun or reflected beam sensors or with very accurate tracking algorithms.

### 2.3.3 Receiver types

The receiver is the component which absorbs the concentrated solar radiation and transfer heat, with of without the help of an heat transfer fluid (HTF), to the engine. Three different subcomponents in this component can be recognize.
The first is the cavity, also known as a second concentrator. It has the goal of further concentrate the sunbeam in a smaller spot. The second one is the receiver itself, the focal spot where the sunlight is concentrated. The third is the Heat Transfer System (the presence of this system depends on the type of receiver considered).

All the receivers for solar dish systems can be classified according to three different categories: Directly illuminated receivers, Reflux Receivers and Volumetric Receivers.

#### 2.3.3.1 Directly Illuminated Tube Receivers

In the first attempts to design solar receiver for Stirling engines, the geometry of the engine's heater tubes was modified to adapt it to absorb the solar radiation. This approach has been successfully used in a large number of dish/Stirling systems [48].

The main problems related to this type of receivers are two. They requires highly accurate concentrators to produce reasonably uniform incident solar flux distribution. The tubes can experience temperature gradients that can degrade the receiver performance and can result in a shortening of its lifetime.

An example of a Direct illuminated receiver is the United Stirling of Sweden AB (USAB) 4-95 receiver used in the Vanguard and McDonnell Douglas dish/Stirling systems whose schematic is shown in figure 17.

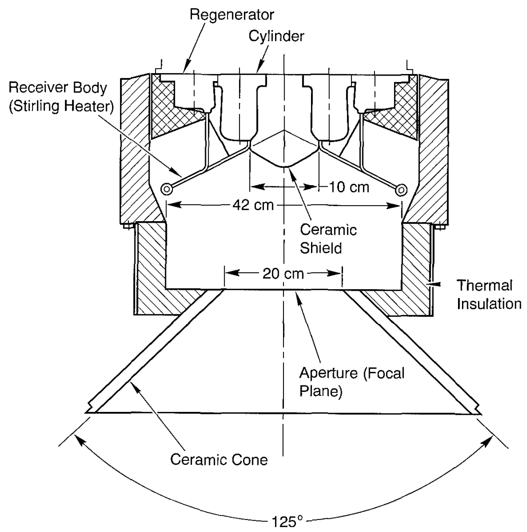


Figure 17: Schematic representation of the United Stirling of Sweden AB (USAB) 4-95 receiver [25]

#### 2.3.3.2 Reflux Receivers

In this kind of receivers the engine's working fluid is not directly heated but an intermediate transfer fluid is used. The HTF is heated up at the absorber where it evaporates. This fluid then evaporates in the heat exchanger tubes of the engine, releasing the corresponding condensation heat. The liquid HTF flows back to the absorber by gravity [48]. The heat transfer fluid is usually a liquid metal (e.g Sodium).

When compared with directly illuminated receivers, an important advantage is the possibility of a nearly isothermal operation even if the incident solar flux distribution is not completely uniform. The reflux receiver permits also a relatively independent design optimization of the absorber and the engine's heat exchanger tubes [9]. Higher engine efficiencies are also possible because of a small difference between the peak temperature and engine working gas temperature [48]

Reflux receivers can further be sub-categorize in two sub-categories. Pool-Boiler receivers and Heat-Pipe receivers.

A Pool-Boiler receiver has the absorber surface always immersed in a pool of liquid metal. An example is shown in figure 18.
A Heat-pipe receiver absorber consists of a high-temperature-alloy dome with a sintered powdered metal or metal fiber wick.
A particular type of heat pipe receiver is shown in figure 19. The way the wick are constructed provide a distribution of pore diameters, rather than a single pore diameter in a more typical metal screen wick. The pore distribution allows vapor generation within the wick rather than just at the wick surface. The large pores make the vapor flow through

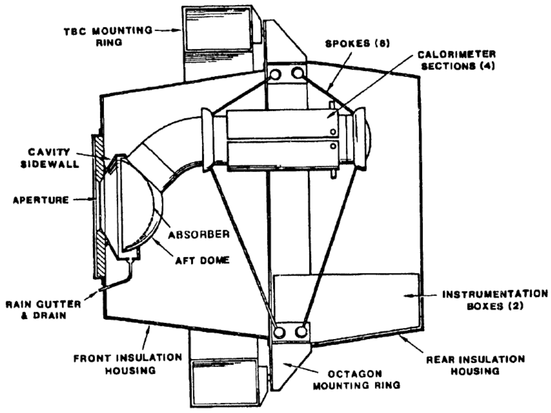


Figure 18: Schematic of a reflux pool-boiler receiver [13]

it while the liquid is free to flow in the smaller pores. This system results in a smaller superheat of the sodium with a thicker wick than the traditional ones.

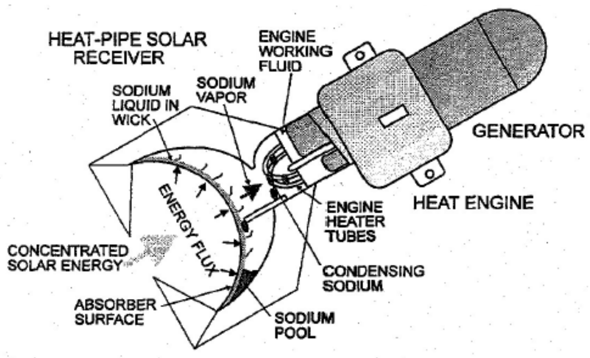


Figure 19: Schematic of a reflux heat-pipe receiver [9]

#### 2.3.3.3 Volumetric Receiver

Volumetric receivers employ porous structures (e.g Honeycoms or porous ceramics). A gas (typically Air) flows through this structures and is heated up to temperature up to 1500°C for SiC materials (up to 1000 for metals and to 1200 for ceramics) [7].
Two basics applications of volumetric air receivers are open-loop atmospheric receiver system for a Rankine cycle and closed-loop pressurized (windowed) receiver system for a Brayton Cycle. The working fluid passes through the porous media thanks to a pressure difference between the two side of the sample generated by a blower [39]. The "volumetric effect" generated by this type of receivers allows the radiation to spread over the volume of the porous material, reducing the local flux density and, consequently, the temperature and the related re-radiation losses.
The atmospheric receivers have been found to suffer from non uniformity flow conditions and persistent local overheating and they were mainly tested on solar tower systems [1].
Examples of closed-loop pressurized (windowed) receiver are shown in figure 20 and 21.

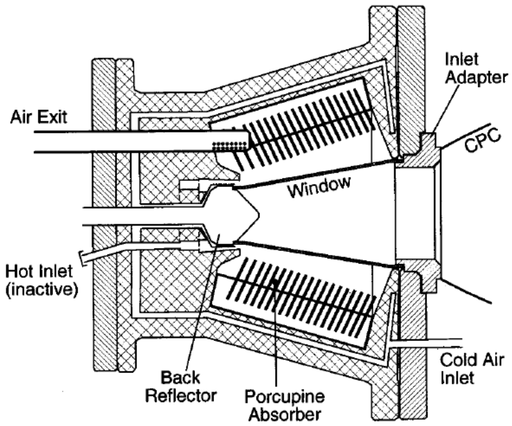


Figure 20: DIARP solar receiver [2]

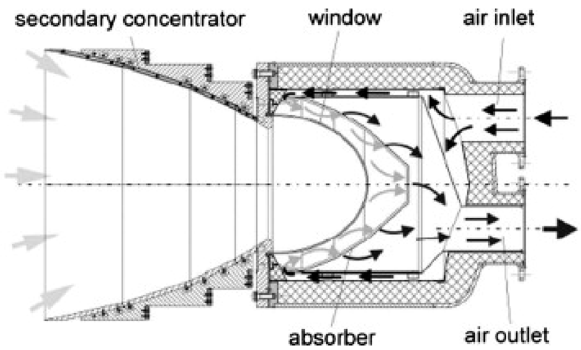


Figure 21: REFOS solar receiver [4]

#### 2.3.4 Engine

The thermal energy gained in the receiver is used as an energy input of a power cycle. Two different types of cycles are mainly used in solar dish application: Stirling and Brayton cycles (the typical gas turbine cycle).

##### 2.3.4.1 Brayton

In the Brayton cycle air is compressed, it is heated up either with an external heat source (as in solar dish systems) or by combustion (Gas turbines). The resulting gas is then sent to a turbine where it expands and produce electricity. In case of coupling with a dish system the external source is the concentrated sunlight and high efficiency can theoretically be reached with the help of recuperators. Typical value for this type of application are pressure ratio around 2.5 and temperatures around 850°C. The predicted thermal-to-electric efficiencies can reach value higher than 30% [25].

##### 2.3.4.2 Stirling

The Stirling cycle is a closed thermodynamic process (The same working fluid is used within the working cycle). The ideal process is based on the combination of isothermal compression and expansion and iso-choric heating and cooling process. This transformation is accomplished trough the used of the mechanism described in figure 22.

The components used are the heated working cylinder, the cooled compression cylinder and a regenerator for intermediate energy storage.
The compression piston pushes the cold gas through the regenerator, that preheat it. The gas is then heated up in the hot space while the regenerator cools down (a). The working gas inside the hot space expands isothermally and absorbs the heat from the hot space (b). During this process it moves the working piston performing work. When the hot piston reaches the Bottom Dead Center and begins to close, the hot gas passes the regenerator (heating it up) and moves into the cold space (c). Then, the working gas is compressed isothermally and transmits exhaust heat to the cold space (d).

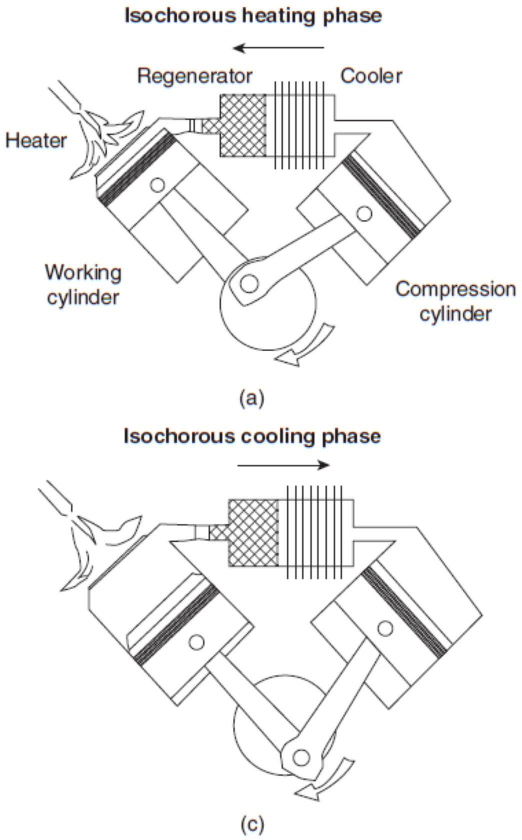


Figure 22: Stirling Engine Working Principle [25]

Usually the regenerator is a highly porous body of high heat capacity that has a considerably larger thermal mass than the one of the working gas. If the displacing piston is coupled to the working piston via a driving mechanism the whole system can serve as a thermal engine [25].

The Stirling engines can sorted in two classes: double acting cylinder or single acting cylinder. In a single acting engine the working fluid contact only with one side of the piston and the working fluid is recirculated between the two cylinders. Two side of the piston are employed in case of a double acting cylinder for moving the fluid from one side to the opposite. The necessity of connection of ducting to a working space with regenerator has made this alternative difficult to be arranged [32].

They can further be categorized into kinematic and free piston Stirling engines. Kinematic engines use a crankshaft mechanism as a power transmission system that can be connected to an electric generator. In case of free piston engine both pistons move freely and the mechanical energy can be converted in electrical energy with the aid of an axial generator. Interior spring damping system are use as mechanical inter-linkage between the two pistons.

This last piston category present the theoretical benefit of a simple structure with high reliability but lag in terms of development when compared to the kinematic one [25].

The engines applied for dish Stirling systems use helium or hydrogen at working gas temperatures between 600 and 800 °C. Power output of the Stirling motor is controlled by varying the working gas mean pressure or piston stroke [25].

## 2.4 Therma Energy Storage: General Classification

Thermal Energy Storage (TES) systems can be classified in three different categories: sensible, latent and thermo-chemical energy storage.

### 2.4.1 Thermo-chemical Heat Storage

Thermo-chemical Heat Storage (TCS) consist in TES system where the energy is stored in form of chemical energy using a reversible chemical exothermic/endothermic reaction. The storage mechanism can be described with the equation 3.

$$A_{(s)} \underset{Heat\ storage\ endothermic\ reaction}{\overset{Heat\ release\ exothermic\ reaction}{\rightleftharpoons}} B_{(s)} + C_{(g)} \tag{3}$$

During the charging process (Endothermic reaction), the solar energy is used to move the reaction from the solid reactant (A) to the solid and gas products (B and C). B and C are stored separately, and, when a discharging is required (exothermic reaction), B and C are placed in contact to react and release the chemical reaction energy between the products stored [26].

Actually, TCS for CSP is based on reversible reactions with high enthalpy of reaction but these reactions presented low efficiency and poor reversibility [26].
Nevertheless, the problem that has been seen from the TCS system prototypes is that the reaction must be reversible and this premises is not being fully achieved and the storage capacity differs from the expected one. This make practical feasibility of such a system difficult to implement with the established premises.

### 2.4.2 Sensible Heat Storage

Sensible Thermal heat storages (STES) consist in TES system where the energy is stored thanks to the temperature change of the selected material. The most important parameters are heat capacity and density of the material.
The amount of energy stored during the process of charge (Q) can be calculated according to the equation 4, where $T_{start}$ and $T_{end}$ are the temperatures before and after the charging phase [K], $c(T)$ is the heat capacity of the material $[\frac{J}{m^2K}]$ as a function of the temperature T, and m is the mass [kg].

$$Q = m \int_{T_{start}}^{T_{end}} c(T)dT \tag{4}$$

A sub-categorization of sensible heat storage in CSP application is shown in figure 23.

The selection of the storage material is the first step when designing the STES. A first categorization can be done distinguishing storages with liquid or solid materials. A second one can be done distinguishing between direct or indirect thermal storages. In case of direct STES, the storage and HTF for a given system are the same, while in case of indirect STES they are different [25].

Examples of Direct liquid storage media are steam accumulator and molten salt two tank storages. The first concept exploit the change in temperature caused by a change

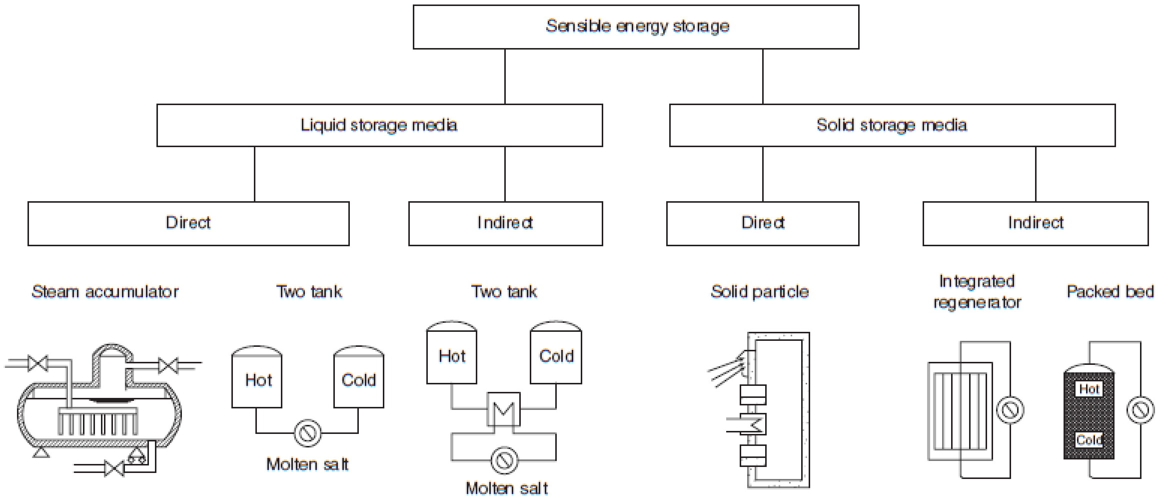


Figure 23: STES classification [25]

in pressure inside a tank where water is present in both liquid and vapor phase. In the second one a liquid medium is cycled between a hot tank and a tank at lower temperature ("cold tank") connected directly to the HTF system. In this case the heat stored is proportional to the temperature difference between the two tank. If the connection is indirect (through the use of an heat exchanger) the system will be an indirect liquid two tank system. Typical fluids used are molten salt or synthetic oils. A direct solid TES can be used in case of solid particles receivers but various issues related to this concept has been found. Examples of indirect solid TES are integrated regenerator and packed bed TES. In the first case, a solid media with integrated heat exchanger is used (e.g. Concrete TES). In the second case particles storage material are packed into a container where the HTF passes through.

### 2.4.3 Latent Heat Storage

Latent Thermal energy storage (LTES) consist in a TES system where the energy is stored thanks to the phase change process. Those systems can be smaller, more efficient and provide a lower cost alternative to sensible heat storage [44].
Between the different forms of phase change process, the solid-liquid transition is efficient in term of volumetric expansion with respect to gas-liquid transition, and higher latent heat with respect to solid-solid transition.
The heat stored in those kind of system can be expressed as in equation 5, where $c_l$ and $c_s$ are the heat capacities of the liquid and solid phase, $\Delta h_{pc}$ is the heat absorbed during the phase change per unit mass $[J/kg]$and $T_{pc}$ is the temperature of the phase change process.

$$Q = m * \int_{T_{start}}^{T_{pc}} c_s(T)dT + m * \Delta h_{pc} + m * \int_{T_{pc}}^{T_{end}} c_l(T)dT \tag{5}$$

The first term in the equation represent the heat that can be stored thanks to the sub-cooling of the solid phase at the beginning of the process, the second term the total heat absorbed during the phase change and the third one is the heat obtainable thanks to the super-heating of the liquid phase.

The development of a latent heat storage system starts with the selection of the phase change material (PCM). The phase change temperature of the PCM should correspond to the temperature required by the system. The phase change process should also be completely reversible without change in the phase change temperature even after a large number of charge/discharge cycles.

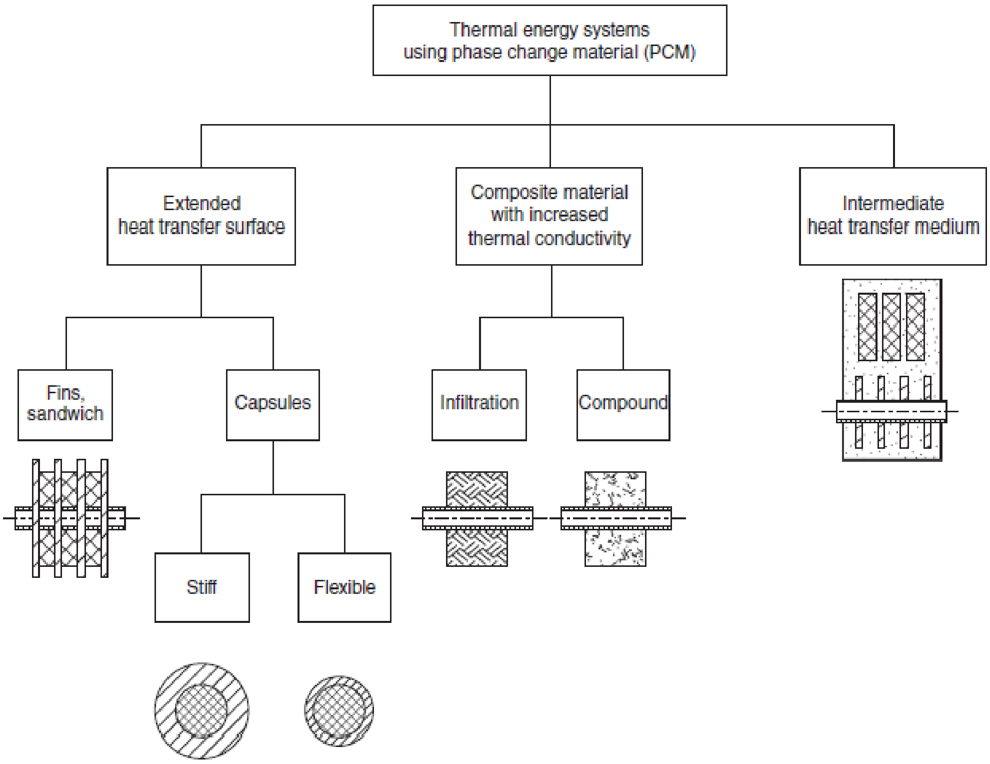


Figure 24: LTES classification [25]

The various PCM storage concept can be distinguished classifying them according to the approach used to increase the heat transfer between the storage material and the heat transfer fluid. A schematic classification can be seen in figure 24.
In a PCM concept with extended heat transfer area, the effective exchange surface is extended by using finned tubes replacing expensive pressure pipes by the less expensive non pressurized thermally conductive structures. Very important is the corrosion resistance of the fins' material with respect to the chosen PCM. Macro-encapsulation of the PCM is another alternative but a significant drawback of this alternative is the necessity to include a gas volume to compensate the expansion of the PCM during melting. Another important drawback is the necessity to have a high quality sealing in the capsules to avoid contamination of the HTF.
An intermediate heat pipe system with a secondary fluid can be used. The heat exchanger area can be smaller. The secondary fluid should undergo a phase change between liquid end vapor phase. During the charging process the secondary fluid in the heat exchanger evaporates and condensate in contact with the PCM, making it melt. During the dis-

charging process the PCM solidified making the secondary fluid condensate in the heat exchanger giving heat to the main heat transfer fluid. Conceptual design have been done considering the coupling with steam cycles.
A composite material with increased thermal conductivity can be obtained with the addition of a material showing high thermal conductivity. Highly conductive particles can be dispersed in the PCM or they can be integrated into matrices made of aluminum or graphite [25].

## 2.5 Thermal Storage Systems in Solar Dish Applications

Conceptual design of thermal energy storage systems in Solar dish application for electricity production is currently under development. Actually two examples of this development have been found in literature.

### 2.5.1 PCM Storage in a Brayton Solar Dish System

The first concept has been developed for a Brayton Solar Dish System integrating a short term storage in the receiver (shown in figure 25).

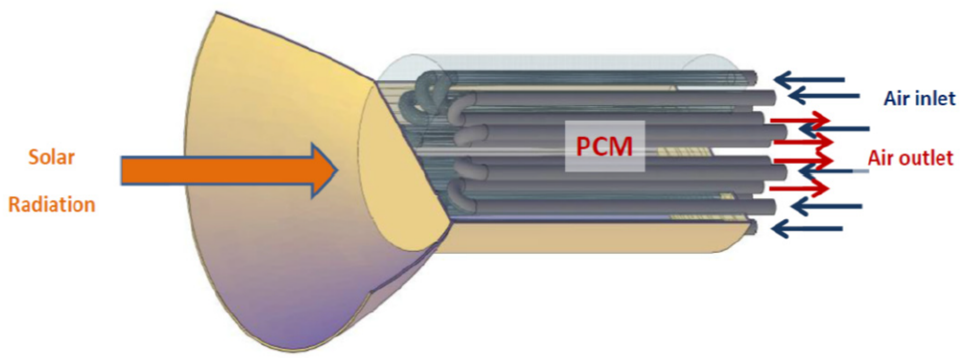


Figure 25: Short term PCM storage for the Brayton system [3]

In the proposed high temperature receiver the compressed air is heated indirectly. The air passes through U-tubes housed in a cylindrical container. The heat exchanger (HX) is a single pass parallel flow HX, similar to the Stirling engine external combustion chamber HX. The U-tube are submerged in the PCM contained inside the solar receiver shell. This small quantity of PCM is just sufficient for a short therm storage system that can compensate the fluctuations of the solar radiation.

### 2.5.2 PCM Storage in a Stirling Solar Dish System

The second concept has been developed for a Stirling Solar Dish System integrating a long term storage (shown in figure 26).

A pump condensate heat pipe transports energy from the solar receiver to the storage media (PCM for high-density isothermal storage) nearly isothermally. A second heat pipe

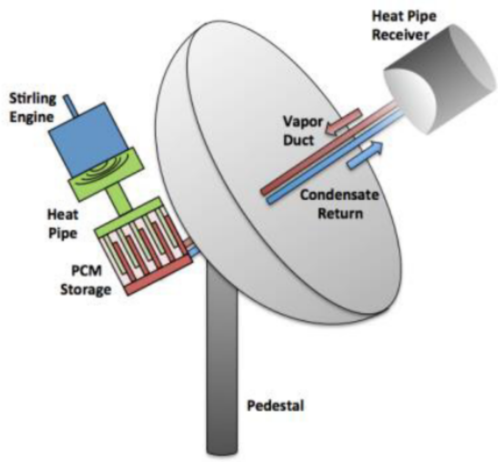


Figure 26: Long term PCM storage integration [10]

transport isothermally the energy from the storage to the engine, providing high flux to the energy through condensation [10]. Those double heat pipe system provide a "Thermal diode effect" reducing thermal losses when operating from stored energy.

Four different interfaces can be recognize. The first one is the solar-to-heat-pipe which require a robust wick system that can distribute the HTF in the receiver. The second and third interface are the heat-pipe-to-storage-media and the storage-media-to heat-pipe. Those last two interfaces require a good knowledge of the dynamic heat transfer characteristic of various stages of PCM melt. The last interface connect the heat pipe to the engine, which is highly design specific.
This system make it possible to provide to the Stirling engines the isothermal input required minimizing the exergetic losses that could results with the utilization of a non-phase-changing material as HTF.

An innovation in this case is obtained by placing the storage media behind the concentrator. In this way the mass of the storage media can be incremented with respect to the condition of placing it in the receiver itself. In this way also the receiver is lighter as long as the engine is no more placed in the receiver, significantly stiffens the dish support structure reducing also the material required in the dish structure.
Another key innovation is the already mentioned Thermal diode effect. Other design have used a single heat pipe that is discharging from the storage in case of no sun. In this case some heat would go to the heater head but some of that will go behind it, suffering energy losses not only from the long heat pipe but also for radiation and convection losses at the receiver. In this design this is avoided by not supplying liquid sodium to the PCM end of the receiver heat pipe preventing significant thermal energy from traveling backward.
Furthermore, the introduction of a heat pipe between the receiver and the engine head make it balance the thermal input between the different cylinder of the engine achieving maximum engine efficiency.

## 2.6 Aluminum alloys as HTES

The choice of the PCM material used plays a key role in the development of the storage and the system itself. Different materials not only features different phase change enthalpies difference but also different phase change temperatures. Temperature around 600 °C are required in dish Stirling systems in order to obtain a suitable power cycle efficiency when operating with the stored energy.
Metallic PCMs offer the potential needed in those kind of high temperature applications with their high density and high thermal diffusivity, which eliminates the need for a large exchange surface [22].

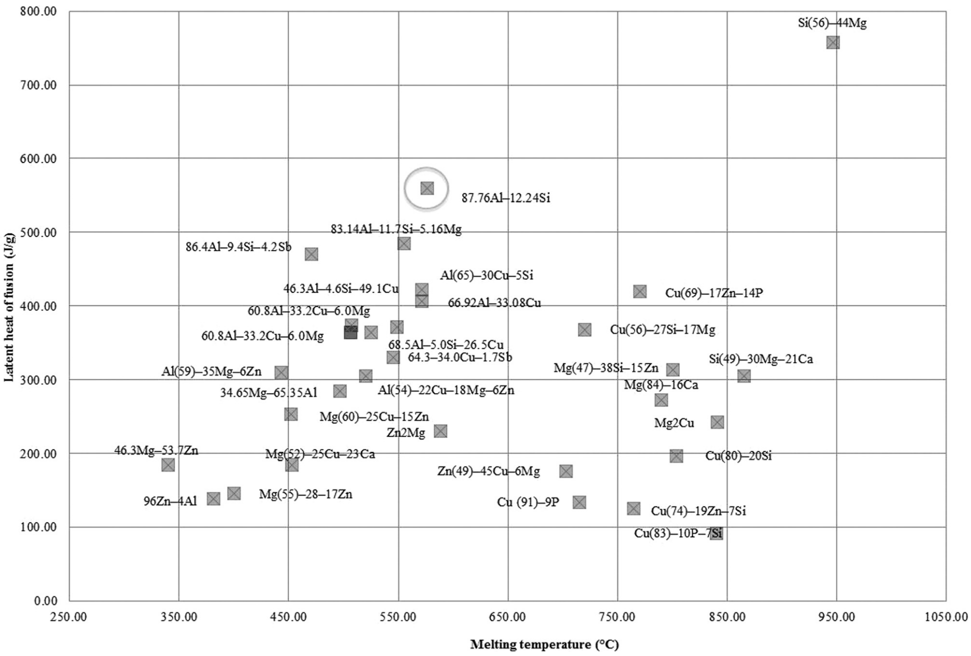


Figure 27: Phase change temperatures and enthalpies for different metallic alloys [22]

Many studies have been carried out to find out which are the eutectic alloys that can better fit the CSP applications. Figure 27 shows phase change temperatures and enthalpy differences for different metallic mixtures.

According to the graph it is possible to identify a eutectic alloy of Aluminum and Silicon as the best metallic PCM candidate with its 560 kJ/kg heat of fusion and 576° melting point. Aluminum alloys have been also found to be relatively stable through multiple heating and cooling cycles, and that having an accurate eutectic composition and controlling cooling rates may improve stability [16]. Other studies have also analyzed the possibility of using non eutectic AlSi alloys (80Al20Si, 70Al30Si, and 60Al40Si) [52], underlining the beneficial operating temperature increase. This would lead also to an increasing latent heat and thermal conductivity. It is important to underline that in those cases, even if the mixtures starts to solidify at temperatures up to 937°C, the complete solidification temperature of all compositions happens at the eutectic transition temperature. Such partial melting could be useful when the carrier fluids go through the storage medium multiple times with progressively changing temperatures.
In the case that will be study, such a solution will not be considered as long as the interest

in the PCM storage is due to the possibility to obtain a nearly-full isothermal input, whit a very narrow phase change temperature range.

Additional studies have analyzed the corrosion properties of those alloys with respect to various ceramic Material [41]. It has shown that the corrosion is negligible in case of $Al_2O_3$, $AlN$ and $Si_3N_4$ surfaces and that it can create problems in case of $SiO_2$ surfaces.

## 2.7 Numerical Modeling of PCM

Various numerical models have been developed during the last years to try to describe the behavior of a material that goes under a phase change process. Those numerical methods can be classified in two big categories: fixed grid and adaptive grid methods ( [43] and [31]).

In the fixed grid methods the governing equation are solved in a fixed numerical grid (or mesh) and the liquid solid interface is modeled by an additional equation describing the melting/solidification process. Those methods can be further classified according to the numerical approach to the phase change behavior in: enthalpy method, apparent heat capacity method, temperature transforming model and the heat source method [43].

The adaptive grid methods can be classified in two different categories: mesh refinement method and moving mesh method. In the first one the model starts with an uniform grid and, at each time step grid points are added or removed to increase the accuracy. The main problem with this method is in the conservation of the data structures since the number of grid points changes over time. In the second method this problem is solved considering always the same number of grid points and moving them to follow the melting front movement [51].
Adaptive grid methods are more accurate for distinct PCM (Solidification of water and pure materials) but they are not suggested for alloys and continuous PCMs, as long as it can lead to an increased computational cost [50].

### 2.7.1 Apparent heat capacity formulation

The heat capacity method simulates the variation in enthalpy due the phase-change process increasing the heat capacity value during this process. The conduction dominate one-dimensional hear transfer apparent heat equation can be written as:

$$\rho C_a(T)\frac{\partial T}{\partial t} = \frac{\partial}{\partial x}\left(k\frac{\partial T}{\partial x}\right) \tag{6}$$

Where $C_a(T)$ is the apparent heat capacity and it can be calculated as follows.

$$C_a(T) = \begin{cases} C_s & T < T_m - \epsilon \\ (C_s + C_l)/2 + L/(2 * \epsilon) & T_m - \epsilon < T < T_m + \epsilon \\ C_l & T > T_m + \epsilon \end{cases} \tag{7}$$

Where $\epsilon$ is half of the fictitious melting temperature range. The thermal heat conduction is then approximated in the melting temperature range as an intermediate value between the heat conduction of the solid phase and the one of the liquid phase.

Different heat capacity and heat conduction approximation methods can be used, with or without a smoothing of the properties, as shown in figure 28.

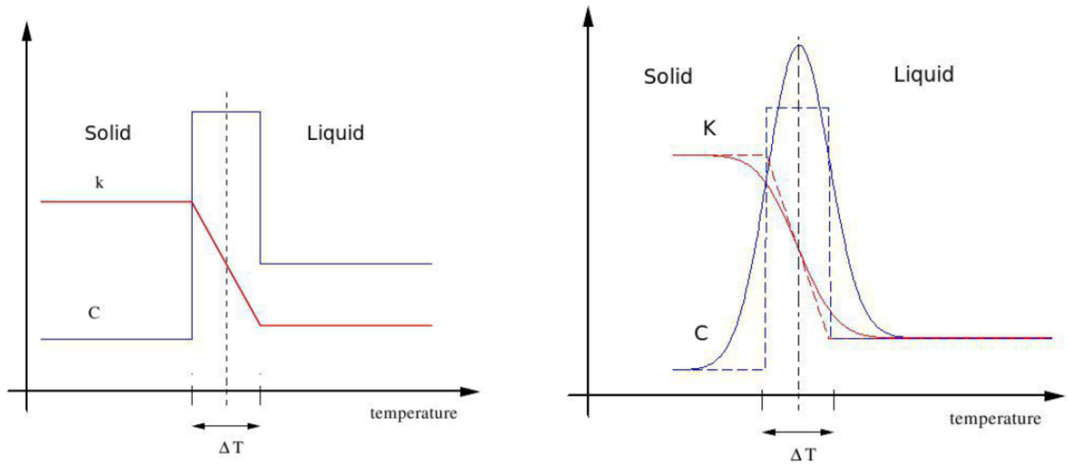


Figure 28: Different heat capacity and heat conduction approximations [31]

In this case the convergence might be an issue if the half phase change range is set too small or the time step is too large as long as there is the possible risk of missing the latent heat contribution [43].

### 2.7.2 Enthalpy method

Another way pf approaching the phase change process in a fixed grid is the use of an enthalpy method. The governing heat conduction equation is expressed as follows:

$$\rho \frac{\partial h(T)}{\partial t} = \nabla(k \nabla T) \tag{8}$$

In this case the problem is solved considering a direct dependence between temperature and enthalpy without considering an equivalent heat capacity.
In case of an isothermal phase change, the enthalpy can be expressed as:

$$h(T) = \begin{cases} cp_s * (T - T_{ref}) & T <= T_{pc} \\ cp_s * (T_{pc} - T_{ref}) + L + cp_l * (T - T_{pc}) & T > T_{pc} \end{cases} \tag{9}$$

This approach creates a discontinuity in the enthalpy function that could lead to numerical issues. A phase change temperature range can be considered (Creation of a mushy region) and the enthalpy can be expressed as:

$$h(T) = \begin{cases} cp_s * (T - T_{ref}) & T <= T_s \\ cp_s * (T - T_{ref}) + f * L & T_s < T <= T_l \\ cp_s * (T_l - T_{ref}) + L + cp_l * (T - T_l) & T > T_l \end{cases} \tag{10}$$

where f is the liquid fraction (That can have a value from 0 to 1) and L is the latent heat expressed in $J/kg$. $T_s$ is the temperature at which the melting process start and $T_l$ is the temperature at the end of the melting process.

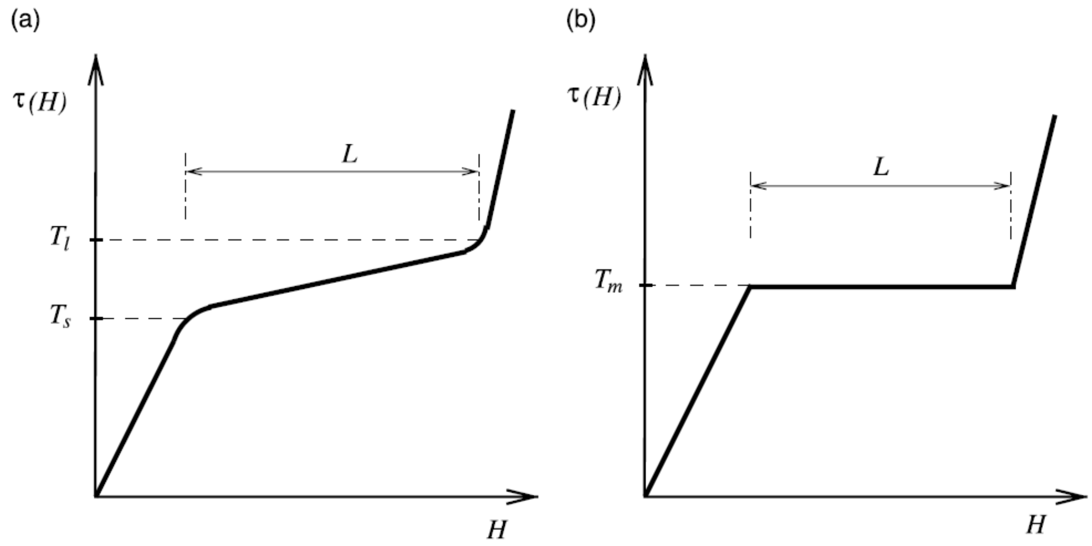


Figure 29: Temperature versus enthalpy relationships: (a) mushy phase change and (b) isothermal phase change [6]

The temperature versus enthalpy relationships in the two different approaches is shown in figure 29.

# 3 Presentation of the system

In this section the simplifications related to the system model of the solar dish system will be presented.

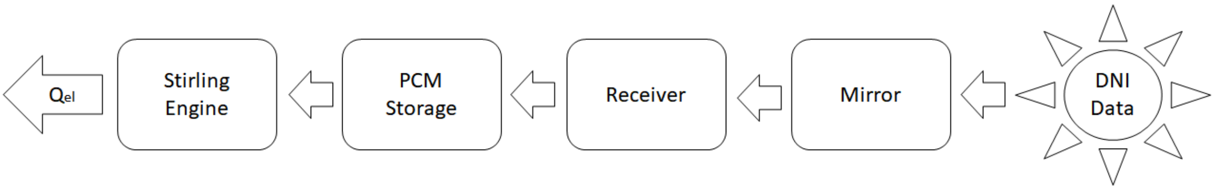


Figure 30: Block representation of the system

## 3.1 Mirror and Receiver Efficiencies

The receiver and the mirror efficiencies in the solar dish system will be considered constant during the study.

$$\eta_{mirror} = 0.95 \tag{11}$$

$$\eta_{receiver} = 0.95 \tag{12}$$

The mirror area will not be considered constant but it will be changed over the various simulations. The receiver efficiency is considered constant even if, in the real case, a change in the receiver temperature would cause a variation of the receiver losses.

## 3.2 Engine Model

The Stirling engine will be modeled considering the following assumptions:

- Minimum temperature acceptable by the engine $T_{min} = 400°C$;
- Ambient temperature: $T_a = 15°C$;
- Efficiency of the Stirling engine proportional to the Carnot efficiency:

$$\eta_{engine} = 0.5 \left(1 - \frac{T_a}{T_h}\right) \tag{13}$$

- Additional parasitic losses in the engine $P_{el,parassitic} = 1kW$.
- Nominal power of the engine $P_{el,nom} = 13kW$.

The engine has been considered to operate at nominal electrical power whenever possible. If the temperature required by the storage to guarantee the nominal power is lower than $T_{min}$, the engine power will be decreased in order to have $T_h$ equal to that threshold.

# 4 PCM modeling

The storage consists of a block of this PCM which is directly heated by the solar radiation concentrated unto the receiver. The heat is then extracted from the storage and send to the Stirling engine through a complex Heat transfer fluid system. Because of company policy, the model of this part of the system will not be disclosed. As a rough simplification, null resistivity between the HTF and the storage and the HTF and the engine will be considered.

Actual CFD simulations on how this system will behave in charge and discharge phase of the storage are still under development and a much simpler model is required by the company to be incorporated in a bigger system model.

Two different models will be developed:

1. The first simplified model consist on a 0D approach where the storage is considered to operate in a quasi steady state condition. In this way it will be possible to describe the system with very simplified equation reducing the computational cost as much as possible. Convection in the liquid layer of the storage will be described using heat transfer correlations available in literature.

2. A second simplified model consist on a Finite Difference 1D approach. In this case the heat transfer in the liquid layer of the storage will be described as pure conduction where the heat transfer coefficient will be scaled according to the value of the Nusselt number obtained through the same correlations used in the previous model.

The material that will be considered for both the models is the eutectic alloy of Al-Si. The properties that will be considered for this particular alloy are presented in table 2.

| Parameter | Symbol | Value |
|---|---|---|
| Solid Thermal Conductivity | $K_s$ | 165 $W/(mK)$ [53] |
| Solid Specific heat capacity | $cp_s$ | 1.16 $kJ/(KgK)$ [53] |
| Solid Density | $\rho_s$ | 2620 $kg/m^3$ [17] |
| Liquid Thermal Conductivity | $K_l$ | 80 $W/(mK)$ [42] |
| Dynamic Viscosity | $\nu$ | $10^{(-3)}(-0.0012T + 1.914)$ mPa*s [27] |
| Liquid Density | $\rho_l$ | $2603 - 0.241 * T\ kg/m^3$ [27] |
| Thermal Expansion Coefficient | $\beta$ | $13.1 * 10^{-5} 1/K$ [24] |
| Liquid Thermal Diffusivity | $\alpha_l$ | 0.3 $cm^2/s$ [40] |
| Latent Heat | $\Delta H$ | $499 kJ/kg$ [17] |
| Phase Change Temperature | $T_{pc}$ | $580°C$ [17] |

Table 2: Al-Si Properties

The liquid thermal conductivity and liquid thermal diffusivity considered are the ones of the aluminum alloy A356 due to the lack of AlSi experimental data, approach suggested by the company.

## 4.1 PCM modeling: first 0D model

In this subsection the developed 0D model will be presented, together with its validation and the results obtained for the operation of the system during a reference day.
The assumptions made for the development of this model are the ones listed below:

1. Quasi-Steady state operation of the system: the temperature distribution in the solid part of the PCM will be considered linear and directly proportional to the heat extracted from the storage;
2. Expansion in the liquid phase negligible: the effect of density variation in the liquid section will be taken into account only when considering the heat transfer coefficient correlations;
3. Storage considered as a rectangular cavity heated from one side and cooled from the opposite one. The upper and the lower part of the storage will be considered adiabatic (negligible heat losses from the storage);
4. Null thermal resistivity between the cooled wall and the heat transfer fluid that goes to the engine;
5. Negligible variation of the internal energy in the solid due to temperature variation;

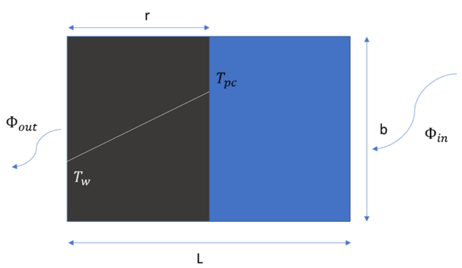


Figure 31: 0D PCM model

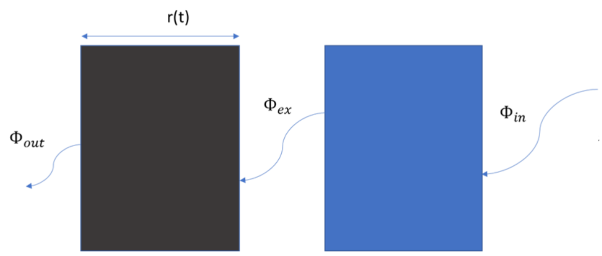


Figure 32: 0D PCM split model

The solid and the liquid part of the storage will be considered as separated blocks that exchange heat between each other and whose dimension are dependent. A final comparison will be done considering the same model but neglecting the internal energy variation of the liquid phase of the storage.

### 4.1.1 Liquid Section

The energy conservation equation considered for the liquid section of the storage is the following one:

$$\Phi_{in} = \Phi_{ex} + \Phi_{liquid} \tag{14}$$

Where $\Phi_{in}$ [W] is the power gained by the receiver, $\Phi_{ex}$ [W] is the power exchanged with the solid part and $\Phi_{liquid}$ [W] is the power used to increase the liquid temperature $T_{liquid}$ [K] plus the power used to bring the melting region from $T_{pc}$ to $T_{liquid}$.

$$\Phi_{liquid} = V\rho c p_l \frac{dT_{liquid}}{dt} + A\frac{dr}{dt}\rho c p_l (T_{liquid} - T_{pc}) \tag{15}$$

$$T_{liquid} = \frac{T_{PC} + T_r}{2} \tag{16}$$

$$V = A(L - r) \tag{17}$$

$$\Phi_{ex} = h_{conv} A (T_r - T_{PC}) \tag{18}$$

Where $h_{conv}$ $[W/(m^2K)]$, the heat transfer coefficient, is calculated accordingly to heat transfer correlations taken from literature.

$$Nu_l = 0.22 * \left(\frac{Pr}{0.2 + Pr} Ra_l\right)^{0.28} * \left(\frac{H}{L}\right)^{-1/4} \tag{19}$$

$$\begin{bmatrix} 2 < \left(\frac{H}{L}\right) < 10 \\ \\ Pr < 10^5 \\ \\ 10^3 < Ra_l < 10^{10} \end{bmatrix}$$

$$Nu_l = 0.18 * \left(\frac{Pr}{0.2 + Pr} Ra_l\right)^{0.29} \tag{20}$$

$$\begin{bmatrix} 1 < \left(\frac{H}{L}\right) < 2 \\ \\ 10^{-3} < Pr < 10^5 \\ \\ 10^3 < \frac{Ra_l Pr}{0.2 + Pr} < 10^{10} \end{bmatrix}$$

The value of the Nusselt number has been considered equal to one when none of those two correlations could be applied.

### 4.1.2 Solid Section

The energy conservation equation considered for the solid section of the storage is the following one:

$$\Phi_{ex} = \Phi_{out} + \Phi_{s1} + \Phi_{s2} \tag{21}$$

Where $\Phi_{out}$[W] is the power going to the HTF, $\Phi_{s1}$[W] is the power used to melt the solid layer and $\Phi_{s2}$[W] is the power used to increase the internal temperature of the solid $T_{solid}$[K].

$$\Phi_{s1} = A\frac{dr}{dt}\rho\delta h \tag{22}$$

$$\Phi_{s2} = A * r * \rho * c_p * \frac{dT_{solid}}{dt} \tag{23}$$

$$\Phi_{out} = A * K * \frac{T_{PC} - T_w}{r} \tag{24}$$

$$T_{solid} = \frac{T_{PC} + T_w}{2} \tag{25}$$

As anticipated in the assumptions, the $\Phi_{s2}$ will be considered negligible

### 4.1.3 Sub-cooling and Super-heating

Even if the sub-cooling and the super-heating of the storage will not be considered in the simulations that will be performed afterwards, a simplified approach for those two condition has been developed for a later use.

An additional variable has been added: the state of charge of the storage (SOC). SOC will be calculated as the equivalent length of the liquid layer divided by the total length of the storage. The equation 22 will be considered even if the value of SOC would be smaller that 0 (Sub-cooled condition) or larger than 1 (Super-heated condition). In those cases the equivalent energy $\Phi_{s1}$ will be considered used either to sub-cool or to super-heat the storage.

When SOC is lower than zero, the storage will be considered completely solid and the temperature at the receiver will be considered equal to $T_{subcool}$. It will be expressed as:

$$T_{subcool} = T_{pc} + \frac{\Delta H}{cp_s} * SOC; \tag{26}$$

When SOC is larger than zero, the storage will be considered completely liquid and the temperature at the wall will be considered equal to $T_{supheat}$ that will be expressed as:

$$T_{supheat} = T_{pc} + \frac{\Delta H}{cp_l} * (SOC - 1); \tag{27}$$

### 4.1.4 Validation

The validation of the code has been done considering as the test case the 2D numerical benchmark presented by Hannoun et al. which involves the melting of a square enclosure subject on one side to a temperature higher then the melting temperature.

In figure 33 the two models results are compared.
The developed model seems to underestimate the increase of the PCM liquid fraction.

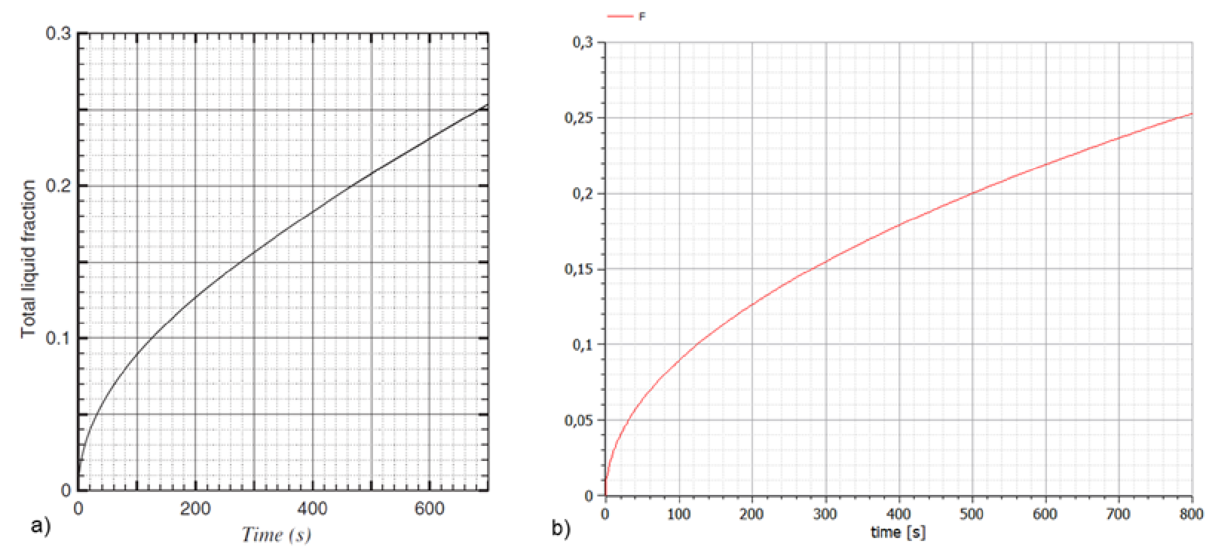


Figure 33: Evolution of the liquid fraction from the 0D model (b) and the Hannoun et al. model [33] (a)

This was expected as long as the melting front in reality doesn't move parallel to the heated wall but will have a different shape due to natural convection loops. This would increase the heat transfer area and, so, the heat exchanged between the liquid and the solid part of the storage.

### 4.1.5 Reference day for the study and Storage Operation

The 1st of January in Abu Dhabi will be considered as the reference day used to analyze the operation of the storage for different aspect ratios.

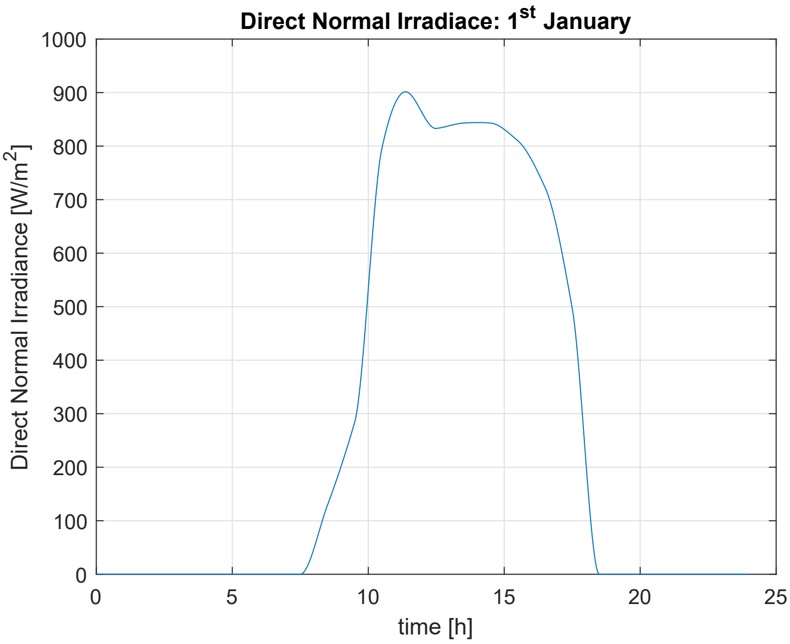


Figure 34: Reference Day Direct Normal Irradiance

The only component of the solar irradiation that will be taken into account during the study is the direct normal irradiance (DNI), as long as this is the only component usable by CSP technologies.

The source of the weather data is the EnergyPlus website [15] and the Modelica model used to upload those data is the model Buildings.BoundaryConditions.WeatherData.ReaderTMY3.

The evolution of this parameter over the day is shown in figure 34.

For the purpose of the study, the storage will be considered to be charged during the daytime and discharged during the night. This has been done in order to observe the behavior of the storage system in both pure charge and pure discharge mode for the different state of charge of the storage.

The variation of the following parameter will be observed:

- Mean efficiency of the system;
- Receiver Temperature;

The mean efficiency of the system will be calculated as the ratio of solar energy hitting the mirrors to electrical energy output from the Stirling engine.
This operation will carried out for different aspect ratio considering a storage size equal to 8 hours.

The storage dimension will be calculated in "hours of storage" ($h_{Storage}$), which are the hour of nominal operation of the engine that the storage can guarantee when it is fully charged (everything is liquefied).

The volume of PCM material for a given number of $h_{Storage}$ will be calculated as:

$$V_{storage} = \frac{h_{storage} * 3600 * P_{el,nom}}{\eta_{nom} * \delta h * \rho_s} \tag{28}$$

The frontal area of the storage will be considered square shaped and the three dimensions of the storage will be calculated consequently.

### 4.1.6 Simulation Results

The results presented below refer to a storage size equal to a 8 hours storage with a mirror area equal to 55 $m^2$.

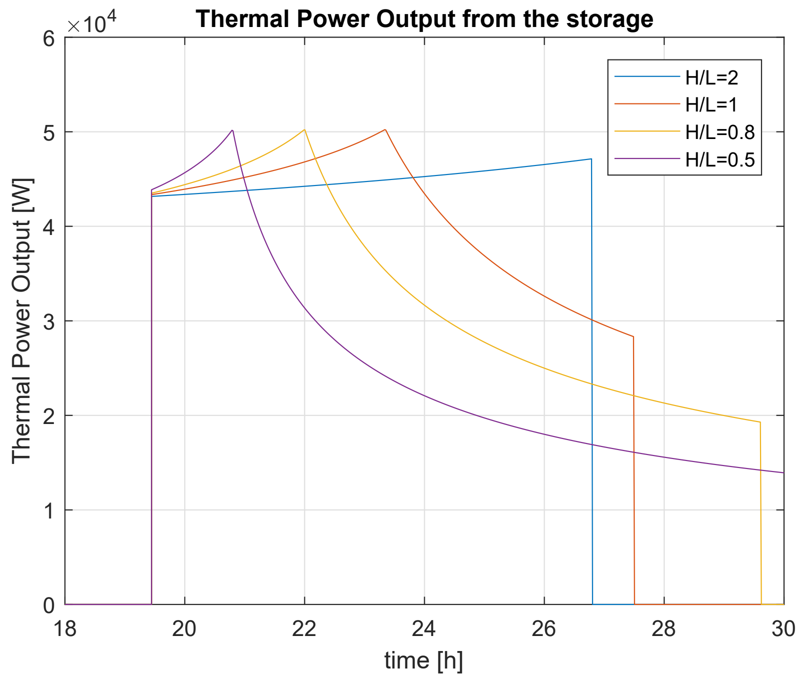


Figure 35: 0D model: Thermal Input to the engine

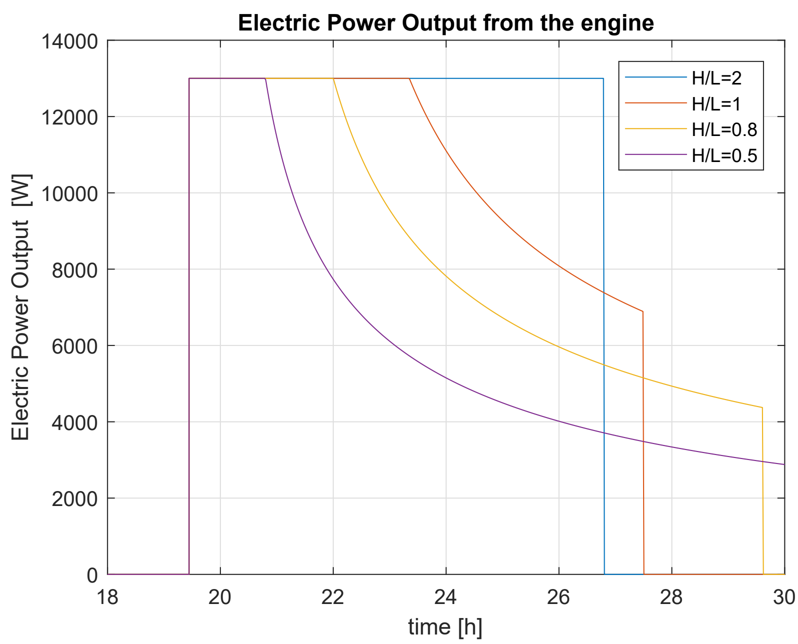


Figure 36: 0D model: Electric Output from the engine

In figure 35 and 36 the thermal and the electric outputs obtained from the model for different aspect ratio are shown.

Two different operation conditions can be recognize. At the beginning of the discharge phase the electric output from the engine is equal to the nominal engine power, while the thermal output is increasing. This is due to the progressive increase of the dimensions of the solid layer that leads to a decrease of the wall temperature, and, so , a decrease of the engine efficiency.

The second operation condition starts when the solid layer reaches a critic value for which $T_w = T_{min}$. In this case, maintaining a constant electrical power output would mean to have a $T_w$ lower than the minimum one, so a constant wall temperature is considered. In this way the efficiency of the engine will be considered constant and both the electric output and the thermal output will be reduced.

The larger is the aspect ratio (H/L), the later this critical value is reached. For an aspect ration equal to 2 the second operation condition is not observed as long as this is never reached during the operation (the critical value is larger than the storage length).

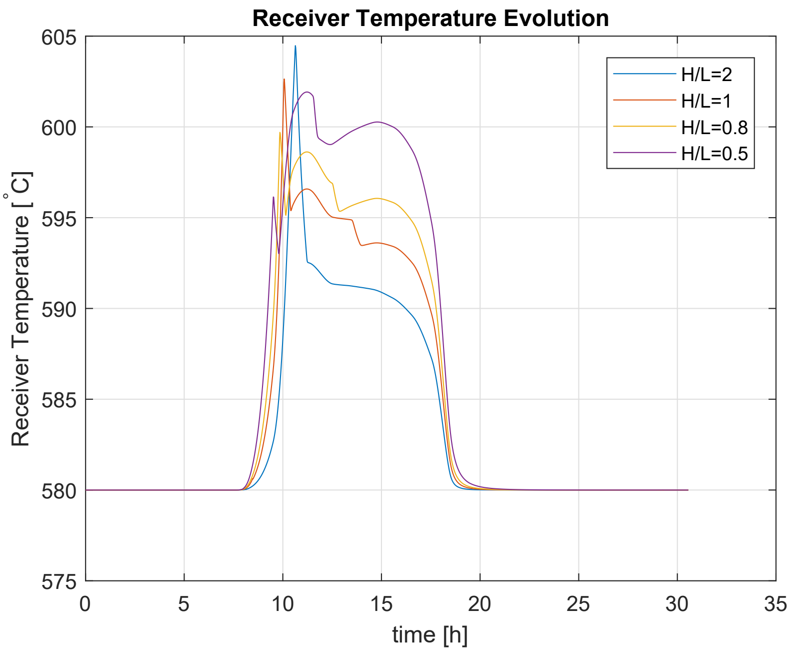


Figure 37: 0D model: Receiver temperature evolution

The receiver temperature over the charging phase is plotted in figure 37. The mean receiver temperature is lower when the aspect ratio is larger. A peak in the receiver temperature is observed, which increase if the aspect ratio is increased. This condition happens when the Nusselt number sharply increase from a value of 1 to a higher value due to the correlations considered.

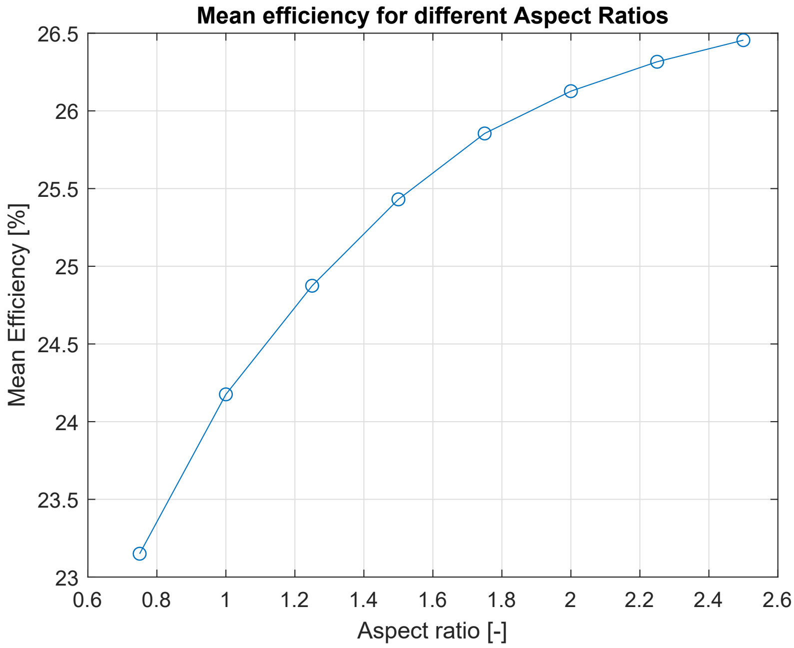


Figure 38: 0D model: Mean efficiency for different Aspect Ratios

In figure 38 the values of the mean efficiency calculated for different aspect ratios are shown.
The higher is the aspect ration, the higher is the mean efficiency of the system calculated. It is important to underline that this model is a simplified model in which neither the receiver area or temperature influence the receiver efficiency. A further analysis of its behavior would be needed to draw more precise conclusions on the best layout from an energy point of view.

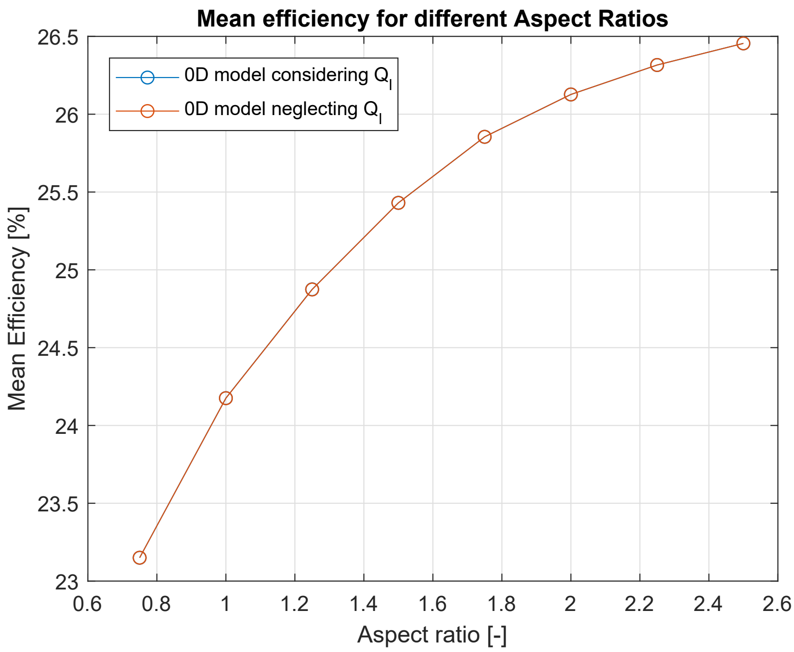


Figure 39: 0D model: Mean efficiency for different Aspect Ratios with and without $Q_l$

In figure 39 a comparison between the engine efficiency obtained with and without considering the variation of the liquid enthalpy is made. As it can be observed, there are not significant efficiency variation (the efficiency point are almost overlapping). The sensible heat accumulated into the system can be considered negligible when compared to the latent heat accumulated in the storage when it comes to evaluating the overall system efficiency.

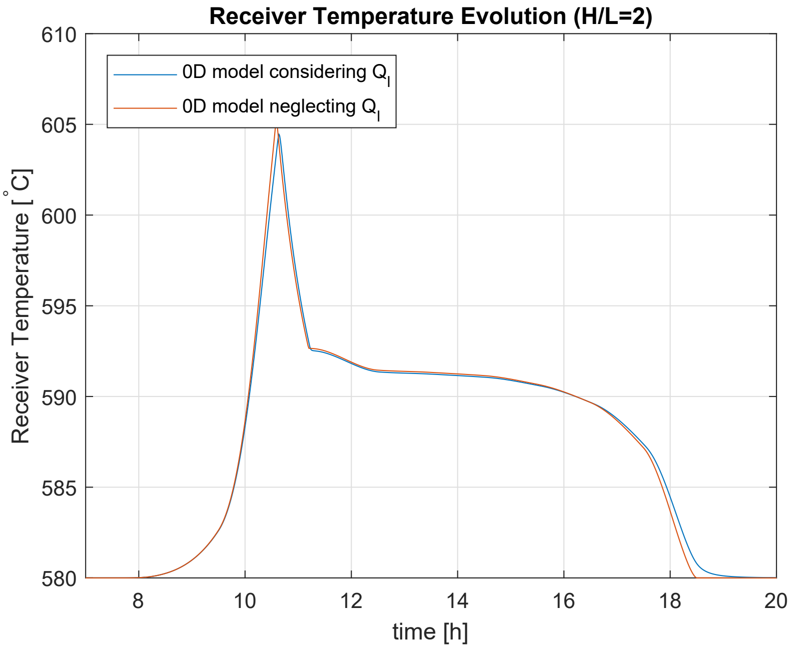


Figure 40: 0D model: Receiver Temperature Evolution for the model with and without $Q_l$

In figure 40 the receiver temperature evolution for an aspect ratio equal to 2 are shown for both the models with and without $Q_l$. The receiver temperatures are slightly different in the two cases (the receiver temperature is slightly higher towards the end of the daylight).

If the PCM storage model has to be inserted into different system models, it would be advisable to use the approach that neglects the $Q_l$ when the receiver efficiency is considered constant in order to further reduce the computational cost, and use the approach that considers it when a more complex receiver model is interfaced.

## 4.2 PCM modeling: 1D equivalent pure conduction FDM model

The second model that has been developed is a 1D Finite Difference Model (FDM) of the storage. The governing 1D equation has been modified in order to take into account the convection term considering the Nusselt correlations used in the previous model.
The discretization has been considered to be homogeneous over the heat flow direction. A schematic of the discretization is shown in figure 41.

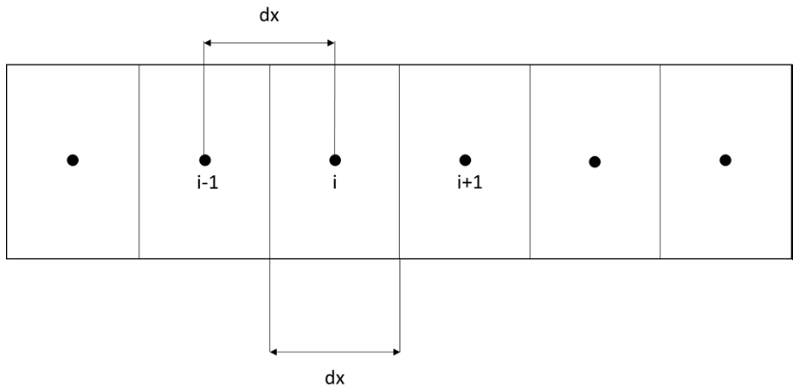


Figure 41: FDM Discretization of the domain

For each node i the discretized energy conservation equation has been written as:

$$\rho * \frac{\partial h_i}{\partial t} = \frac{k_{i-1}+k_i}{2}\frac{T_{i-1}-T_i}{dx^2} + \frac{k_{i+1}+k_i}{2}\frac{T_{i+1}-T_i}{dx^2} \tag{29}$$

The first term on the right-hand side can be considered as the heat exchanged between the node i and the node i-1, the second therm as the one exchanged between the nodes i and i+1. The phase change process has been considered to happen in a very small temperature range of length $2\epsilon$ in order to avoid discontinuity in the enthalpy function.

The model is base on an enthalpy method. The enthalpy has been written as:

$$h_i = \begin{cases} cp_s * (T_i - T_{ref}) & T <= T_{pc} - \epsilon \\ cp_s * (T_i - T_{ref}) + f * L & T_{pc} - \epsilon < T <= T_{pc} \\ cp_s * (T_{pc} - T_{ref}) + f * L + cp_l * (T_i - T_{pc}) & T_{pc} < T <= T_{pc} + \epsilon \\ cp_s * (T_{pc} - T_{ref}) + L + cp_l * (T_i - T_l) & T > T_l \end{cases} \tag{30}$$

The liquid fraction for each node has been calculated as linearly dependent on the node temperature.

$$f_i = \frac{T_i - (T_{pc} - \epsilon)}{2\epsilon} \quad T_{pc} - \epsilon < T <= T_{pc} + \epsilon \tag{31}$$

The heat conductivity for each node has been calculated as:

$$k_i = \begin{cases} k_s & T <= T_{pc} - \epsilon \\ k_s * (1 - f) + k_{l,eq} * f & T_{pc} - \epsilon < T <= T_{pc} + \epsilon \\ k_{l,eq} & T > T_{pc} + \epsilon \\ & \end{cases} \tag{32}$$

The $k_{l,eq}$ is the equivalent heat conductivity of the liquid phase. This is calculate as the effective heat conductivity of the liquid multiplied by the Nusselt number value.

Two Neumann Boundary Conditions have been considered at the first and at the last node (at the receiver and at the HTF wall respectively). The resulting equations are the following ones.

$$\rho * \frac{\partial h_i}{\partial t} = k_1 \frac{T_r - T_i}{dx^2/2} + \frac{k_2 + k_1}{2} \frac{T_2 - T_1}{dx^2} \tag{33}$$

$$\rho * \frac{\partial h_{end}}{\partial t} = \frac{k_{end-1} + k_{end}}{2} \frac{T_{end-1} - T_{end}}{dx^2} + k_{end} \frac{T_w - T_{end}}{dx^2/2} \tag{34}$$

### 4.2.1 Grid Dependence Study

A validation process has been first carried out showing results very similar with the one obtained with the 0D model.
A grid dependence study has been carried out in order to chose the appropriate number of nodes to be used in the numerical simulations. The charging phase in the day studied with the previous model has been considered and both the receiver temperature at 60000 seconds and the mean efficiency at the end of the simulation have been considered for a storage size of 8 hours and an aspect ratio (H/L) equal to 2.

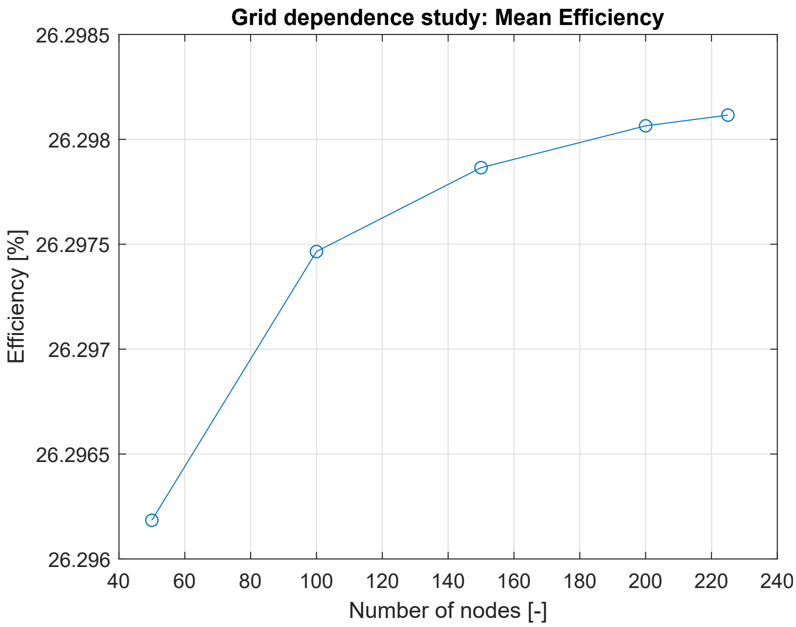


Figure 42: Grid dependence study FDM: Mean Efficiency

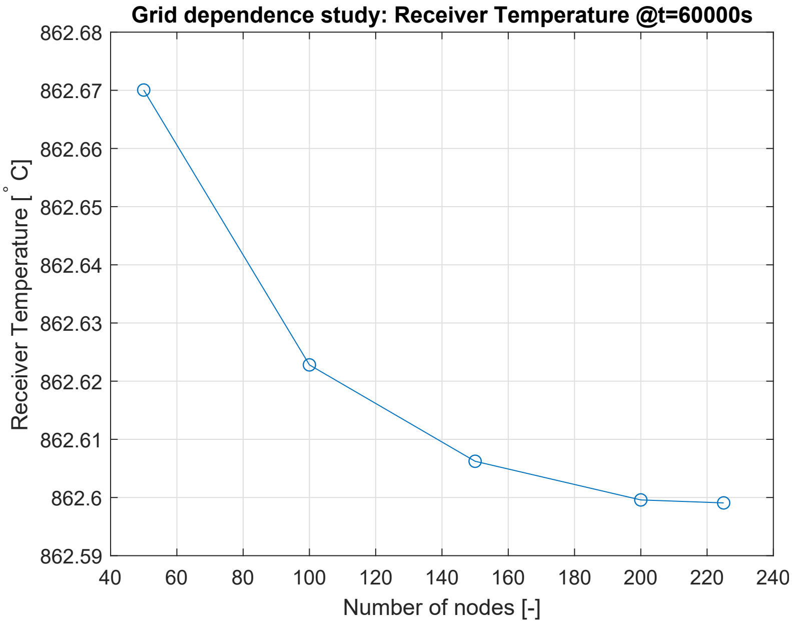


Figure 43: Grid dependence study FDM: Receiver temperature

In the figures 43 and 43 the results of the study are shown. The number of grid points that will be considered now on are equal to 200.

#### 4.2.2 Simulation Results

The storage size considered in this study is an eight hour storage, as the one considered in the previous model. Hereafter some results obtained through the FDM model will be presented together with some comparisons with the first 0D model.

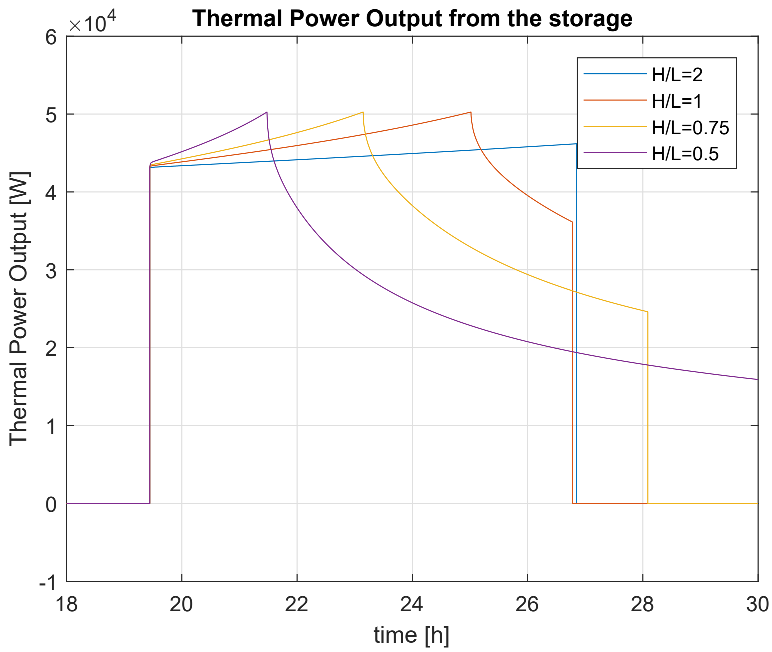


Figure 44: FDM: Thermal Output from the storage

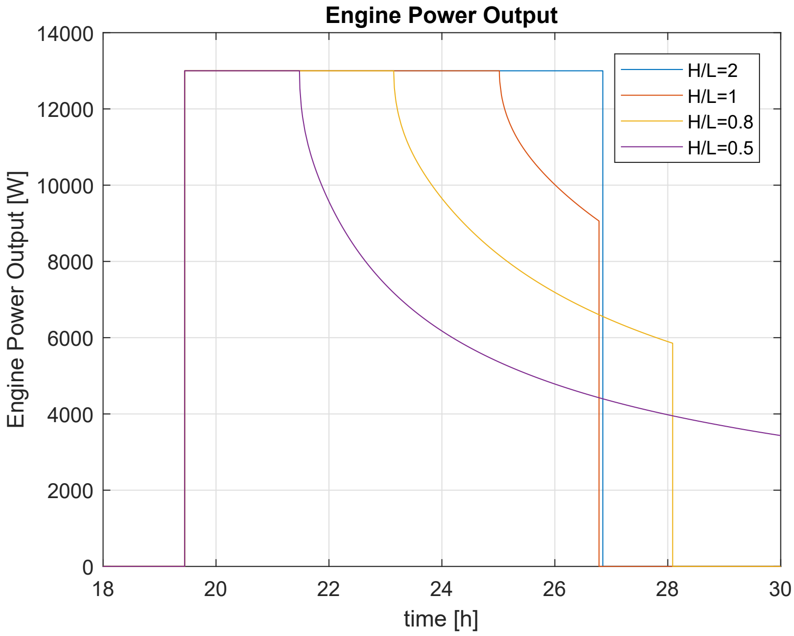


Figure 45: FDM: Engine Power Output

In figure 44 and 45 the thermal power output from the storage and the engine power output for different aspect ratios are shown. The results show similarity between the one obtained with the simplified 0D model. Also in this case the two operational conditions can be recognized and the increase of the value of the aspect ratio increases the duration of the first operational condition, where the electric output from the engine is maintained constant.

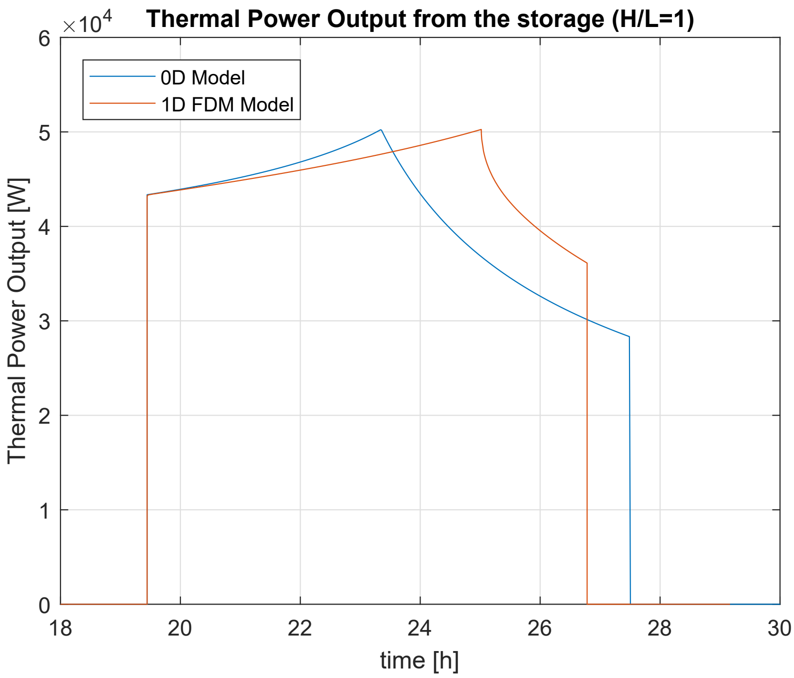


Figure 46: FDM vs 0D: Thermal power output from the storage (H/L=1)

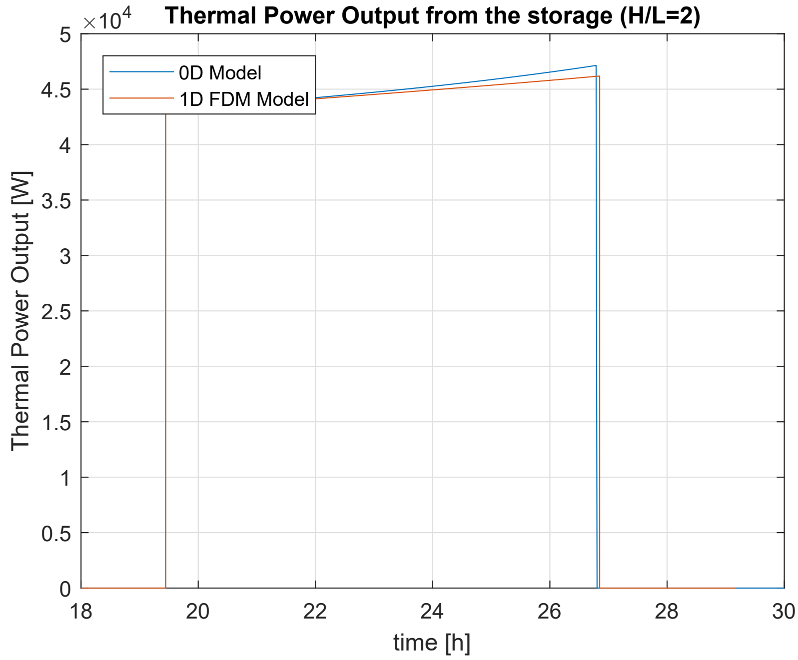


Figure 47: FDM vs 0D: Thermal power output from the storage (H/L=2)

A closer look into the results of both the 0D and 1D analysis is needed to captures the differences and similarities between the two models.

In figure 46 and 47 the thermal power output calculate with the two models for two different aspect ratios are shown.

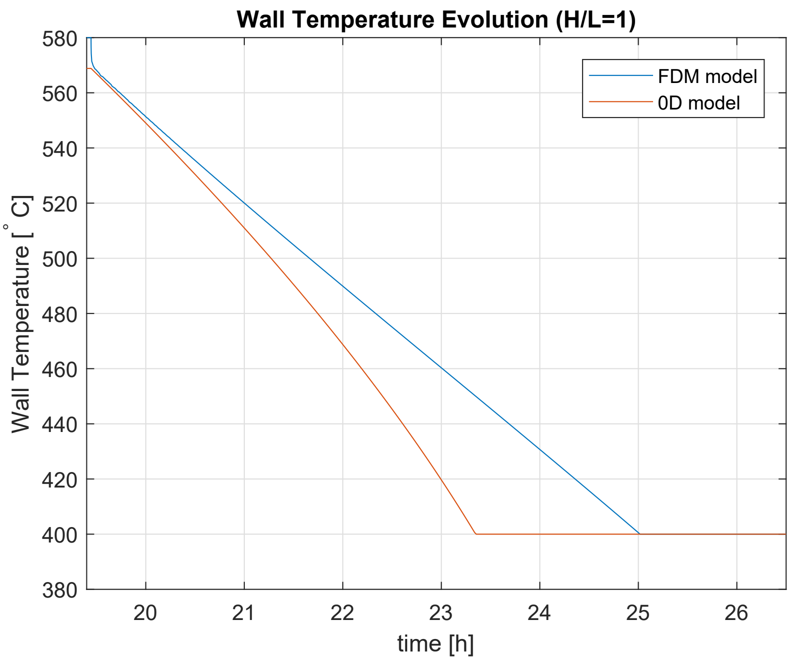


Figure 48: FDM vs 0D: Wall temperature evolution in the discharge phase

It can be noticed that the duration of the first discharge phase is larger in the 1D model with respect to the 0D. This is due to the fact that, in the FDM model, enthalpy variation of the solid layer of the storage are considered, and the time needed to reach a quasi-steady state condition is not neglected. It means that the wall temperature will decrease more slowly with respect to the previous model, increasing the engine efficiency and, so, decreasing the thermal power output needed from the storage to obtain a constant engine output. In figure 48 this temperature behavior can be observed.

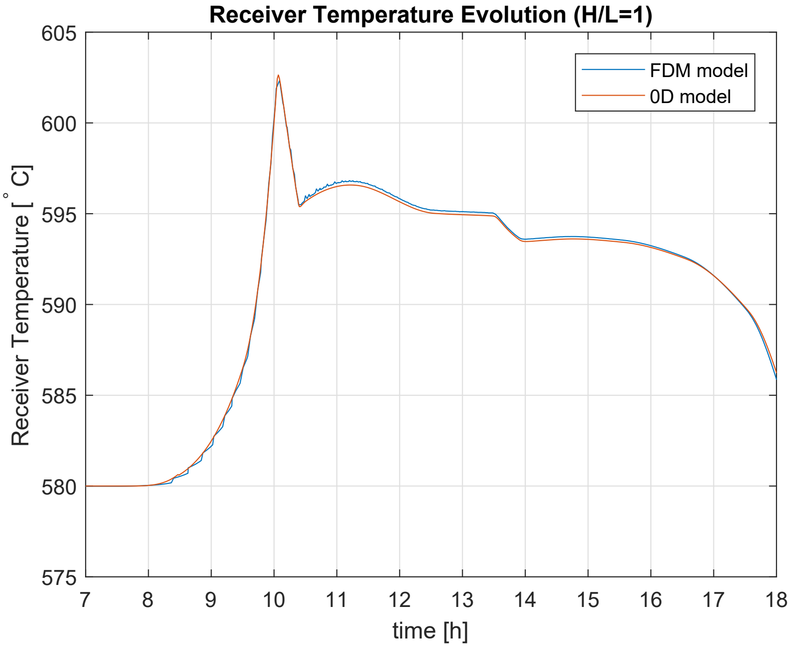


Figure 49: FDM vs 0D: Receiver Temperature evolution (H/L=1)

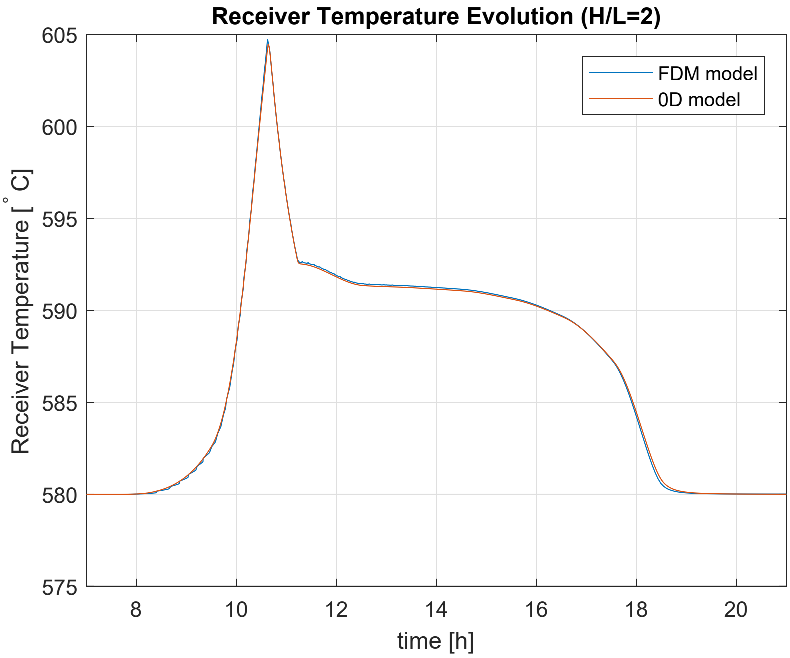


Figure 50: FDM vs 0D: Receiver Temperature Evolution (H/L=2)

In the figures 49 and 50 the receiver temperatures calculate with the two models for two different aspect ratios are shown.
It can be noticed that there are no significant differences between the two models when it comes to the receiver temperatures. In fact, during the charging phase, no temperature variation in the solid layer are achieved and all the energy is used to both heat up the liquid and melt the solid phase.

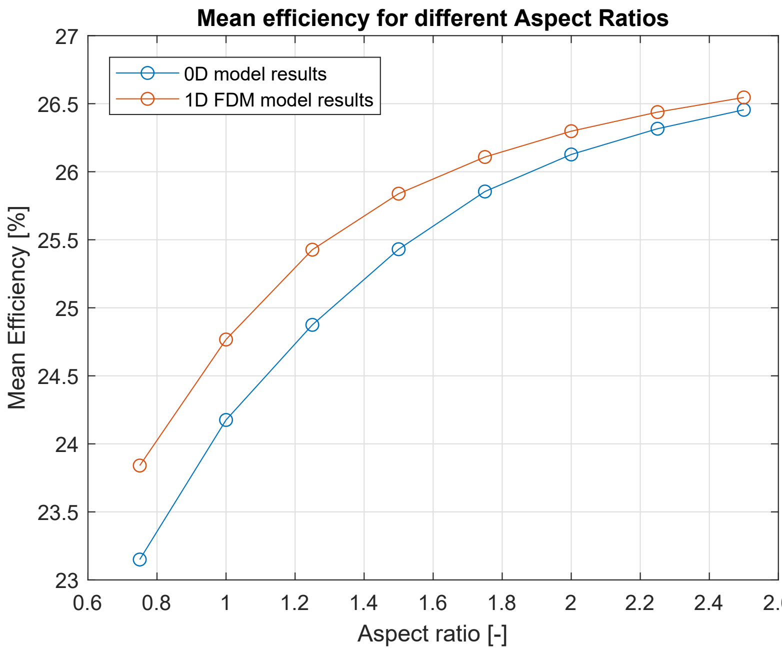


Figure 51: FDM: Mean Efficiency for different aspect ratios

In figure 51 the mean efficiency calculated for different aspect ratios with the two different models is shown. As it ca be noticed. The higher the aspect ratio, the higher the mean efficiency for both the models. An higher efficiency is reached considering the more complex model.

The computational cost of this FDM model is much higher with respect to the one of the model described in the previous subsection and it makes difficult to run a year round simulation for the evaluation of the revenues obtainable. For this reason in the successive section, the first 0D model will be considered, knowing that it represents a more conservative approach with respect to the more complex FDM model (there will be an underestimation of the electrical energy produced during a year).

# 5 Dispatch Control Strategy (DCS)

In this section the Dispatch Control Strategy (DCS) developed in order to run a pre-feasibility study will be presented.
The required input and boundary conditions will be analysed and, subsequently, the Pre-Simulation and the During-Simulation Controllers will be shown, together with their relative Flow Charts.

## 5.1 Required Input and Boundary Conditions

The input required by the DCS developed are the following ones:

1. Tariff Scheme for the chosen location: the dispatch control strategy developed doesn't need to know if there are prioritized operation hours;

2. Nominal Operating Condition of the engine;

3. DNI (Direct Normal Irradiation) during the simulation year;

4. Total power gained by the solar dish per square meter mirror area during every operational day ($J/(m^2)$).

The DNI file will be used in a separate OpenModelica simulation in order to obtain the forth input.
The Pre-Simulation Control Strategy will need only the Tariff scheme, on the contrary, the During-Simulation Control Strategy will need only the last three input.
The normal operating condition of the engine considered in the successive simulation are: $T_{hot,source} = 580°C$, $P_{parassitic} = 1kW$ and $P_{el} = 13kW$.
The nominal thermal power of the engine ($P_{th,nom}$) has been calculated accordingly to the following equation:

$$P_{th,nom} = \frac{P_{el} + P_{parassitic}}{\eta_{T_{hot}=580°C}} \tag{35}$$

This parameter will be used in the During-Simulation Control Strategy.

## 5.2 Pre-Simulation Control Strategy

The first part of the control strategy (the so called "Pre-Simulation Control Strategy") has been developed in Matlab.
The goal is to obtain an output file that will be used in the successive "During-Simulation Control Strategy" to decide when to produce or not.
The simulation year will be analysed considering it split in intervals of 24 hours each.
For each hour, the number of successive hours present in the interval that have a higher price of electricity will be saved. This parameter will be called "Value_hour" or "importance".
One important user defined input to the controller is the parameter "ShiftHours".

This parameter is used to decide if the 24 hours intervals will exactly coincide with the day of the year (if ShiftHours=0) or not. If Shift hours is set to a value "N", the 24 hours interval will be considered to start on the N hour of the analysed day and finish on the N hour of the successive day. This could be useful if there are price peaks during the night.

The code logic is shown in figure 52.

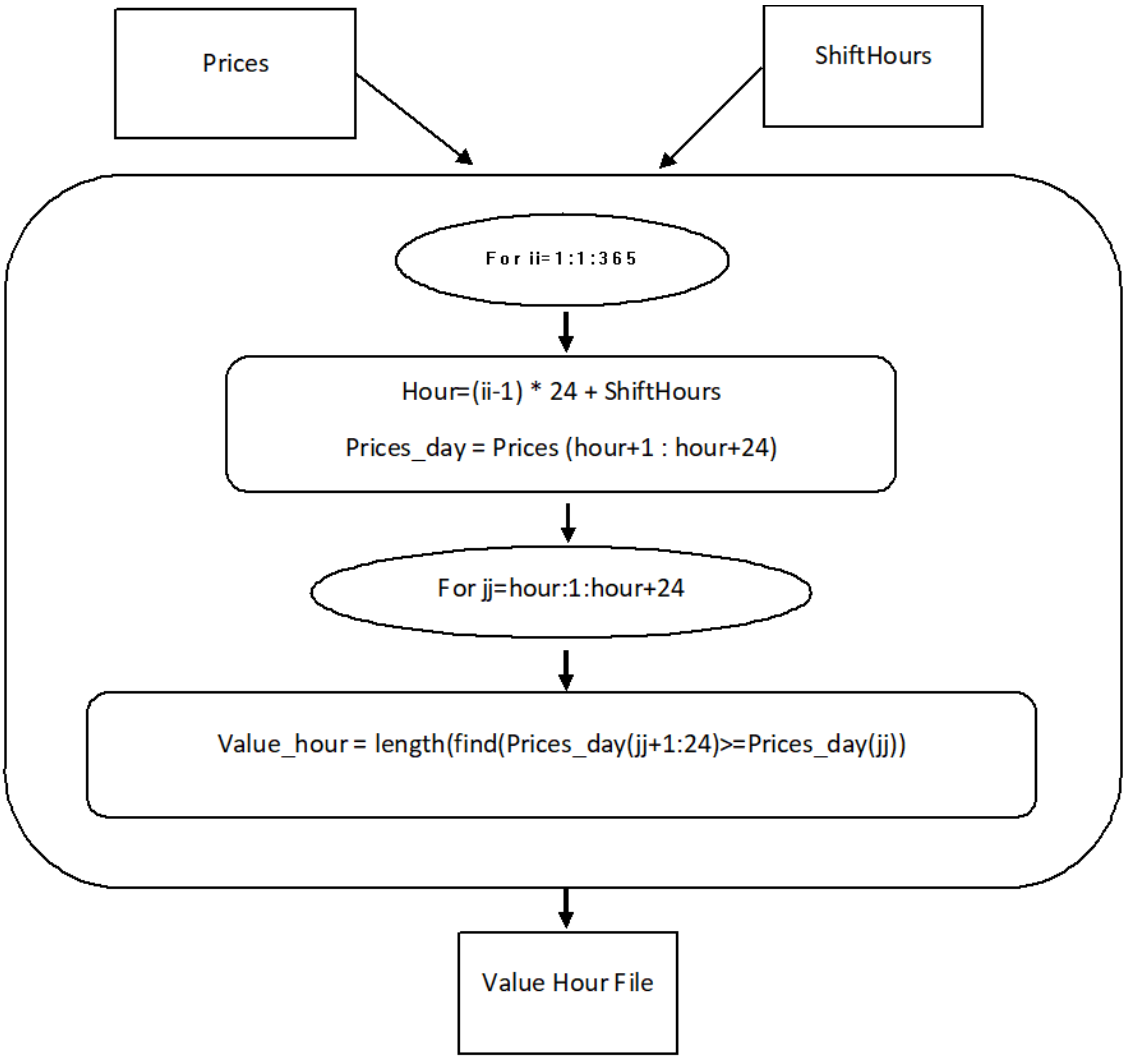


Figure 52: Pre-Simulation control strategy: flow chart

## 5.3 During-Simulation Control Strategy

The real decision on when to produce or not is actually done during the OpenModelica Simulation, through the decision of the value of the "ALFA" parameter. This parameter can have value 1 if the plant will produce energy, or 0 if it will not.
The results obtained from the Matlab simulation will be considered as an input of the model.
Some parameter need to be defined before discussing the algorithm logic. The parameter $Q_{day,left}$ represents the amount of energy gainable by the solar dish in the successive

hours of the day. It is calculated as the difference of the total energy gainable during the analysed day and the one already gained.
The parameter $Min_{disp}$ represent the minutes of nominal operation that can be obtained considering both the energy stored in the system and the $Q_{day,left}$. This is calculated according to the following equation:

$$Min_{disp} = \frac{Q_{day,left} + Q_{th,stored}}{P_{th,nom}} \tag{36}$$

The parameter $Min_{acc}$ represent the minutes of nominal operation that can be obtained considering only the energy stored:

$$Min_{acc} = \frac{Q_{th,stored}}{P_{th,nom}} \tag{37}$$

The parameter $SOC$ represent the state of charge of the storage and it is calculated as the ration between the energy stored and the maximum energy storable into the system.

$$SOC = \frac{Q_{th,stored}}{Q_{th,max,storable}} \tag{38}$$

The decision Flow Chart is shown in figure 53.

The first block in the flow chart is used to see if the energy accumulated into the system plus the remaining energy gainable from the sun is enough to run the system for a number of hour equal to the importance of the analyzed hour plus 40 minutes ( this is done in order to ensure a continuous production of the system and not a continuous turn on and off).
If it is enough, the productivity parameter Alfa will be set to one, else the algorithm continues with the next block.

The second block check if the previous condition is verified without considering the surplus of 40 minutes. If this is true and the previous production parameter was equal to one, the new production parameter will be set equal to one.

The last three blocks are used to avoid to have a fully charge storage that could cause a waste of the gainable solar energy.
The parameter Alfa is set to one if the State of charge is higher that the nominal thermal power multiplied by a factor Zeta, which will be set to 1.17.
If this condition is not meet, Alfa is set to one if the State of charge is higher then 0.94. and the discharge continues until the SOC becomes smaller that 0.9.

If none of the previous conditions is verified the production parameter is set equal to zero.

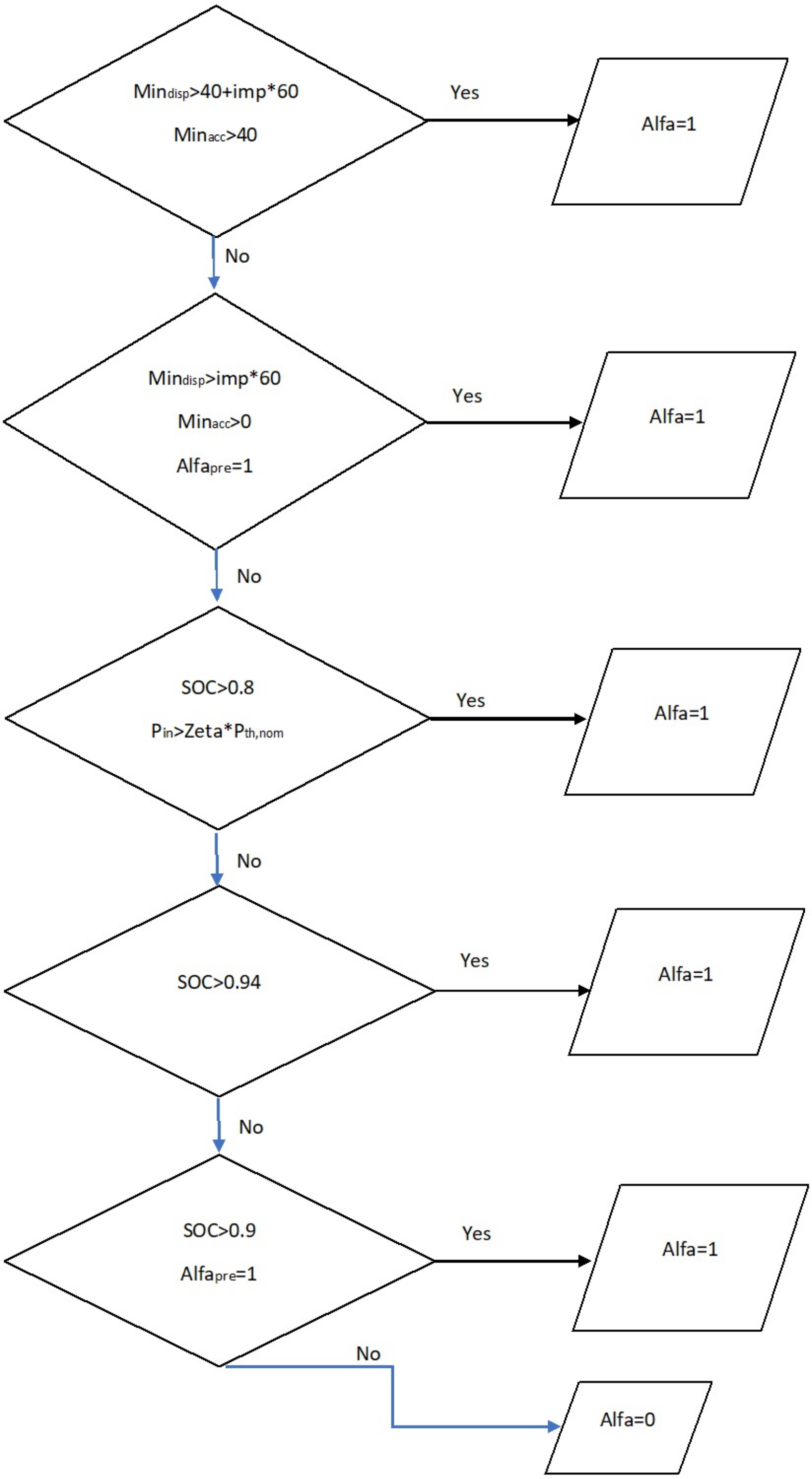


Figure 53: During-Simulation control strategy: flow chart

## 5.4 Performance Indicators

In order to verify the effectiveness of the control strategy, four different èerformance indicators has been considered.

The first performance indicator is called "Economical Effectiveness" (EE) of the control strategy. It is the ratio between the revenues obtained with the developed control strategy for a certain mirror area and hours of storage ($Revenues_{real}$) and the Revenues that could be generated day by day if all the energy gained by the mirrors is used in nominal condition to generate electricity in the hours with the higher electricity price.

$$EE = \frac{Revenues_{real}}{Revenues_{ideal}} \tag{39}$$

The second performance indicator is the so called "Capacity Factor" (CF). It is the ratio between the electrical energy generated by the system in the considered year ($Q_{el,generated}$), expressed in kWh, divided by the energy that could be generated if the system would operate at nominal condition for all the 8760 hours of the considered year.

$$CF = \frac{Q_{el,generated}}{P_{el,nom} * 8760} \tag{40}$$

The third performance indicator is called the "Waste Factor" (WF). It represents the ration between the solar thermal energy lost by the system and the thermal energy gained by the storage. The energy is lost because, when the storage is full, the excess energy is not gained by the receiver.

$$WF = \frac{Q_{th,wasted}}{Q_{th,gained}} \tag{41}$$

The fourth performance indicator is the economical capacity factor. It is the ratio between the revenues obtained from the Solar Dish System and the maximum revenues obtainable considering the plant operating at nominal condition for 8760 hours in a year $Revenues_{max}$.

$$CF_{eco} = \frac{Revenues_{real}}{Revenues_{max}} \tag{42}$$

Al those performance indicators will be calculated in the next section.

# 6 Thermo-Economic Analysis: Boundary Conditions

In this section the boundary conditions for the Thermo-Economic Analysis of the studied system will be presented. The Location selection and the presentation of the analysed year will be done.
Then the costs considered in the evaluation of the CAPEX and OPEX of the system will be shown together with the incentives that could be obtained from the Australian government.
The methodology used for the evaluation of the Internal Rate of Return (IRR) and the LCOE of the system will be considered.

## 6.1 Location selection and analysed year

The location has been selected considering South Australia as a area of study.
The decision has been done considering various parameters such as flat terrain, proximity to the national grid and the location Direct Normal Irradiation (DNI).

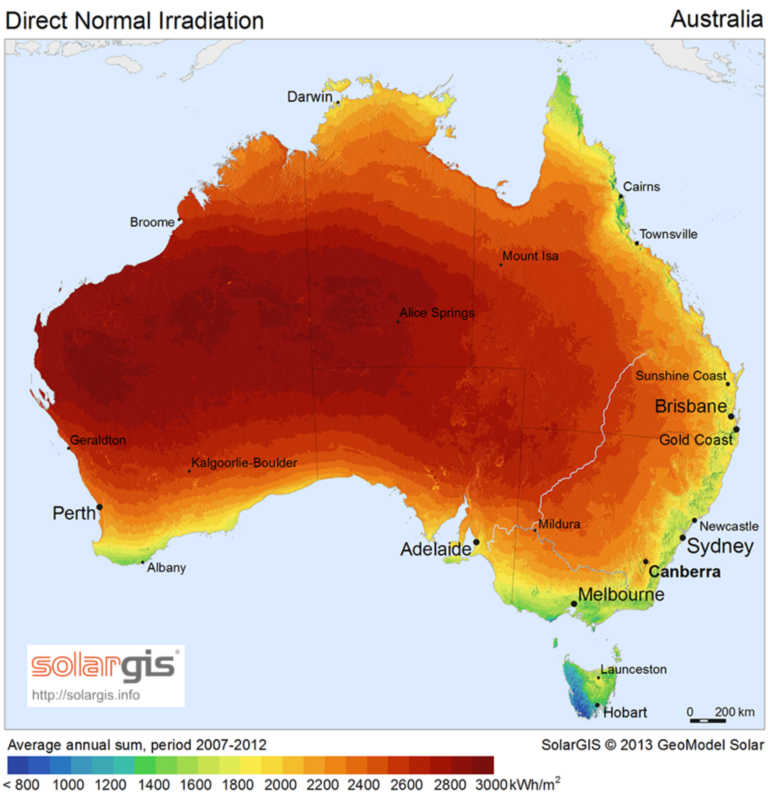


Figure 54: DNI: Australia Map [46]

According to figure 54 the higher DNI is read in the north east part of the considered area. A CSP power plant placed in that region would lead to higher productivity of the plant. The problem of such location would be the connection to the national grid.

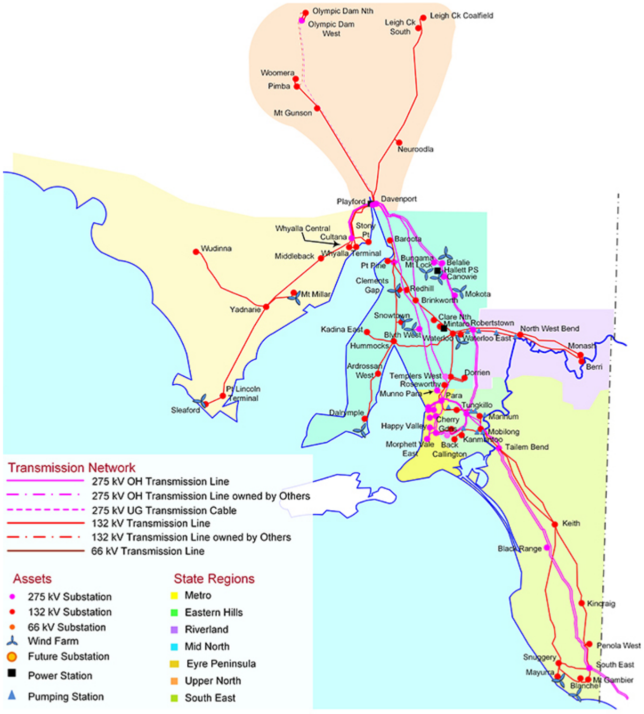


Figure 55: South Australian National Grid [14]

As it can be seen in figure 55 the national grid in South Australia is developed only in its south part. Among the various location, the city of Woomera will be considered due to the proximity to a national grid substation, its flat terrain and the relatively high DNI (equal to 2380 $kWh/m^2$).

The day by day DNI for the selected location is shown in figure 56.

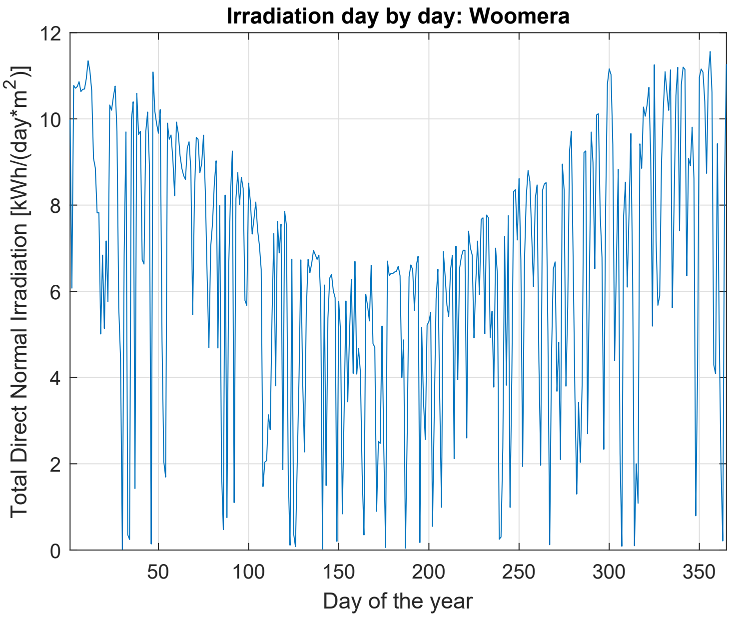


Figure 56: DNI day by day: Woomera [15]

The variation of the electricity prices during the analyzed year expressed in Australian dollar per MWh are shown in figure 57 (Historical Data for South Australia).

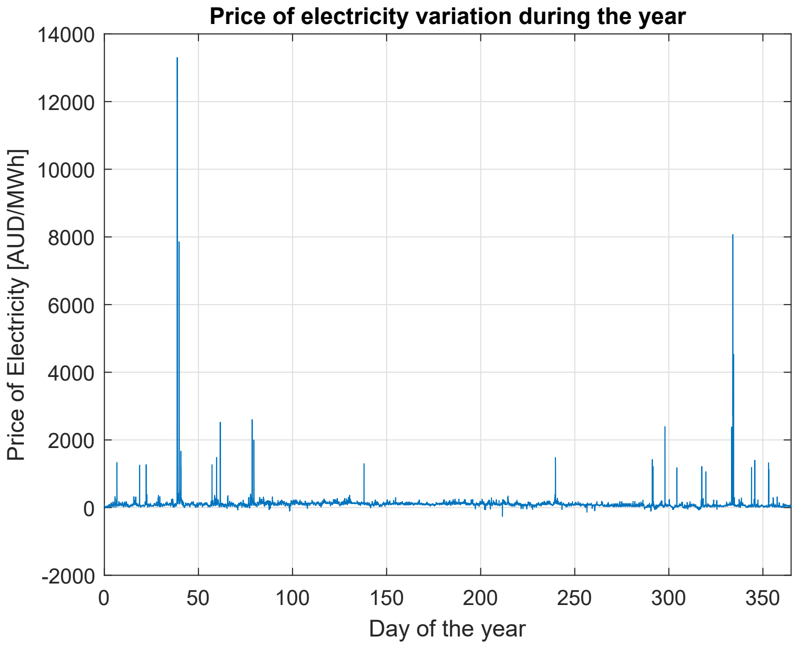


Figure 57: Prices of Electricity

The peaks play a central role in the thermo economical analysis as long as the control strategy for the system has been designed in order to try to produce during those peaks to maximize the obtainable revenues.

## 6.2 System Costs

In this subsection the cost considered during the analysis will be presented. The component costs used are shown in the table below.

| Component | Value | Unit |
|---|---|---|
| Engine | 200 | €/$kW_e$ |
| Generator | 35 | €/$kW_e$ |
| Cooling | 30 | €/$kW_e$ |
| Control | 35 | €/$kW_e$ |
| BOP | 300 | €/$kW_e$ |
| Storage (fix cost) | 2449.1 | €/dish |
| Storage (variable cost) | 16.3271 | €/$kWh_{th}$ |

Table 3: Dish Components Costs

The costs related to the Engine, Generator, Cooling, Control and BOP are taken from the reference [19].

The storage cost has been taken from the reference [8]. The fixed cost have been scaled linearly with respect to the nominal net electrical power of the system with respect to the one considered in the article. The uncertainty related to the prices of the storage is relatively high. For this reason a sensitive analysis on the effect of the variation of those prices will be carried out.
The receiver cost has not been taken into account because the storage system and the receiver represent, in reality, a unique block.

The mirrors cost is calculated accordingly to the cost function developed in the reference [18] presented in the Appendix.

The other costs (EPC, Project Development, Financing and Allowances) are considered equal to 19.5% of the total CAPEX [21].
The OPEX has been considered equal to 36.75 €/(kW*year) [8] and the decommissioning cost equal to 1% of the CAPEX.

## 6.3 Incentives

Although the main economical study will be done considering no incentives for the considered system, a final comparison between the cases with and without it will be presented, considering the effect that they have on the optimal design.
In Australia the incentives for Large-Scale Renewable Energy power plant are obtained through the creation of large-scale generation certificates (LGC) [5].
They are created accordingly to the amount of the eligible renewable energy generated by the system. As a guide, one large-scale generation certificate is equal to one megawatt hour of eligible renewable electricity produced [5].
The value of a LGC is strongly dependent on the market situation: they can be bought and sold by traders and business through the open LGC market. Their value during the 2017 has oscillated between 75 and 90 Australian dollars. During the comparative analysis that value will be considered constant and equal to 80 Australian dollar.

## 6.4 Methodology

Two economical performance indicators will be used during the study: the Levelized Cost Of Electricity (LCOE) and the Internal Rate of Return (IRR) of the investment.

The LCOE is calculated accordingly to the following formula.

$$LCOE = \frac{\alpha * CAPEX + OPEX + \beta * C_{dec}}{E_{net}} \tag{43}$$

The values of $\alpha$ and $\beta$ are obtained considering the following equations.

$$\alpha = \frac{(1 + WACC)^n * WACC}{(1 + WACC)^n - 1} + k_{ins} \tag{44}$$

$$\beta = \frac{WACC}{(1+WACC)^n - 1} \tag{45}$$

The value of $k_{ins}$ will be neglected during the study and the value of WACC will be considered equal to 5%.

The value of IRR is calculated accordingly to the following equation.

$$-\sum_{t=0}^{n_{con}-1} \frac{CAPEX}{n_{con}(1+IRR)^t} + \sum_{t=n_con}^{n_{con}+n_{op}-1} \frac{Revenues - OPEX}{(1+IRR)^t} - \sum_{t=n_{con}+n_{op}}^{n_{con}+n_{op}+n_{dec}-1} \frac{C_{DECOMMISION}}{n_{dec}(1+IRR)^t} = 0 \tag{46}$$

Both $n_{con}$ and $n_{dec}$ are considered equal to 1 and $n_{op}$ equal to 20 year.

# 7 Results and discussion

In this section the results analysis will be carried out. Initially the results obtained for the IRR and LCOE of the system will be shown, indicating the different impact of the variation of both the storage size and the mirror area of the solar dish. Then the operational strategy performance indicators will be analyzed as a function of those parameters.

Secondary a parametric study will be carried out in order to study the effect on both the economical indicator of the variation of the mirrors and the storage costs. The effect of the application of national incentives will be also considered in the last section of the study. Lastly, the effect of a different location choice will be analyzed.

The storage will be modeled with the 0D model neglecting the variation of the liquid enthalpy. This choice has been done in order to reduce as much as possible the computational cost of the simulations as long as we are considering the receiver and mirror efficiencies as constants.
The parameter $ShiftHours$ presented in the Control Strategy section will be considered equal to 5 hours in all the simulation in order to make it possible to take advantage of eventual price peaks present during the night. A storage aspect ratio of 2 will be considered.

## 7.1 Main Study Results

In figure 58 the effect of different storage dimensions and dish aperture area on the Internal Rate of Return of the system is shown.

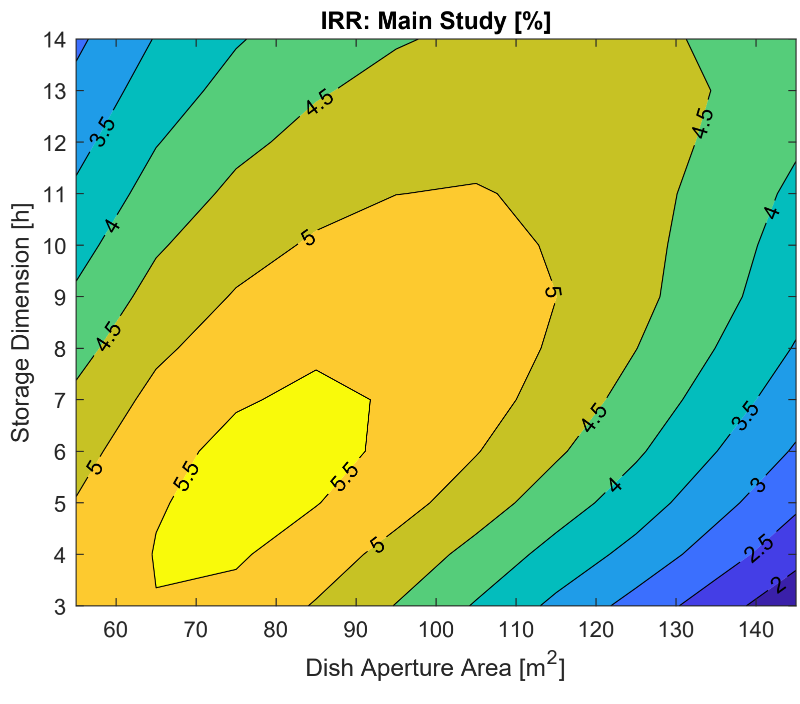


Figure 58: IRR: Woomera

As it can be notice, the higher IRR values are shown to be in the region with storage size smaller than 8 hours and dish aperture area smaller than 90 $m^2$. The optimal layout is shown to happens with a 5 hour storage and a dish aperture area of 75 $m^2$.
The further increase of the dish aperture area would lead to a reduction of the IRR as long as the variation of the mirrors cost it is not covered by the increase in revenues: the control strategy is already able to produce during the price picks.
It is important to underline that those results are very case dependent, a variation in the tariff scheme would lead also to a variation of the optimal configuration.

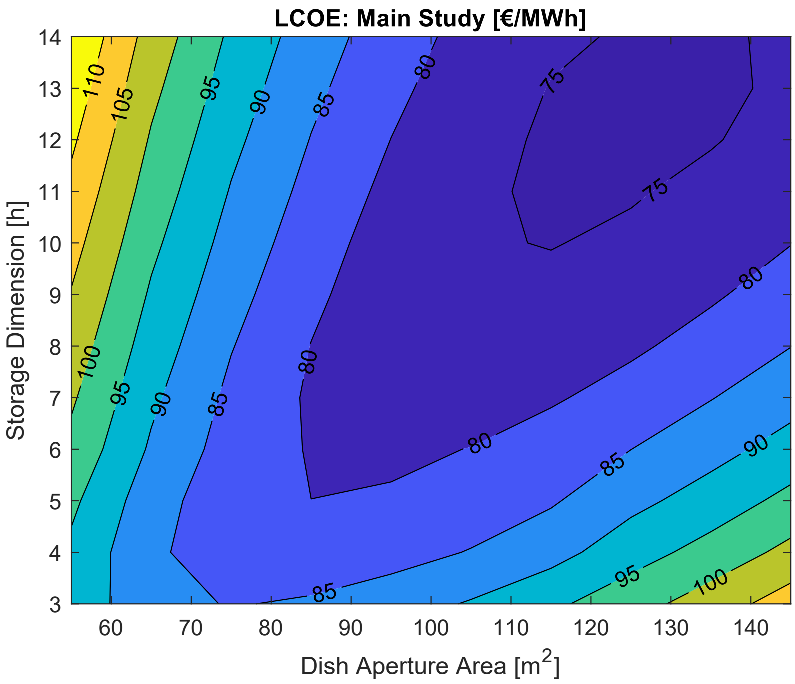


Figure 59: LCOE: Woomera

In figure 59 the variation of the LCOE is shown. It is very important to underline the large difference in the optimal configuration resulting from the two economical performance indicator. While the IRR has the maximum in the lower left part of the graph, the LCOE has its own in the higher right part of the graph, for high storage sizes and mirror areas.

This difference between the two optimal configurations is due to the tariff scheme. A fluctuating price of electricity lead to a higher importance of the moment in which the plant is producing electricity rather then on the quantity of energy generated.
A flat tariff scheme it is more likely to show IRR maximum values very similar to the one shown in the LCOE study.

In the figures 60 and 61 the two performance indicators WF and EE are shown for the different storage sizes and mirror areas. The percentage of wasted energy increases when the dish aperture area increases for small storage sizes. The percentage becomes negligible when the storage size increases.

The Operational strategy Performance Effectiveness shows high values, from 70 to 94%. It underlines the capacity of the developed strategy to catch the high peak present in the tariff scheme.

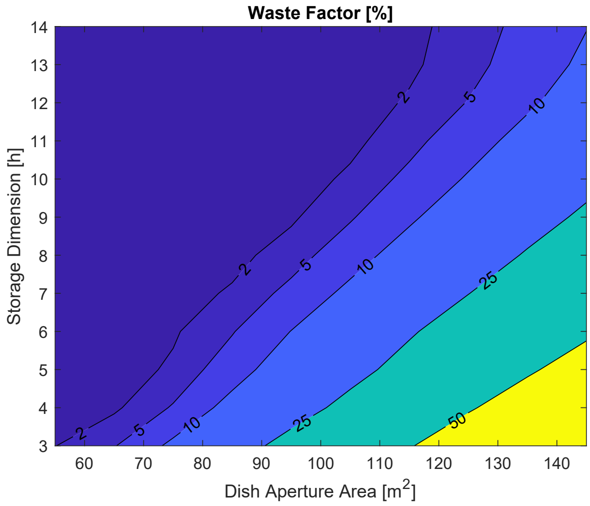


Figure 60: Waste Factor: Woomera

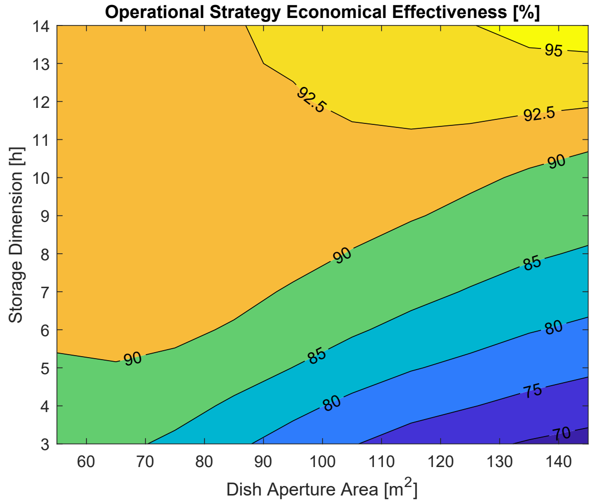


Figure 61: Economical Effectiveness: Woomera

In the figures 62 and 63 the capacity factor and the economical capacity factor for the different combinations are shown.

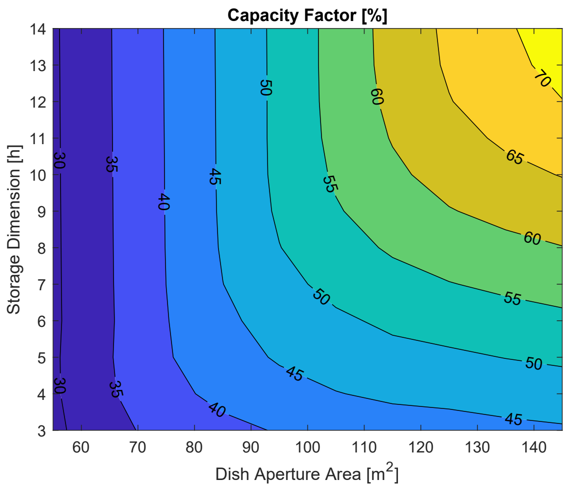


Figure 62: Capacity Factor: Woomera

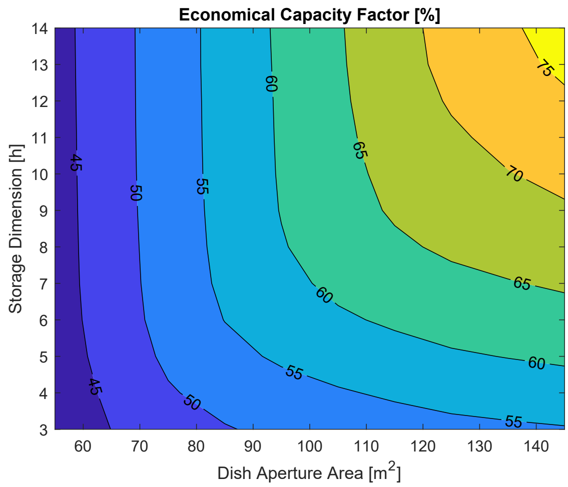


Figure 63: Economical Capacity Factor: Woomera

A comparison between the two graphs is fundamental to understand the difference that has been discussed before between the LCOE and IRR. As it can be notice, an electrical capacity factor of 40% correspond to an economical capacity factor higher than 50%. If the CF is increased by 30% with respect to tha value, the variation in the economical CF is less then 25%.
It underlines the fact that, increasing mirrors area and storage size cold have a positive

effect on the LCOE (as long it is considering the energy generated and not the revenues generated from them) but a negative one on the IRR.

## 7.2 Sensitivity analysis: Storage Cost

The effect of a variation in the storage cost has been studied varying is value by +10% and -10%.

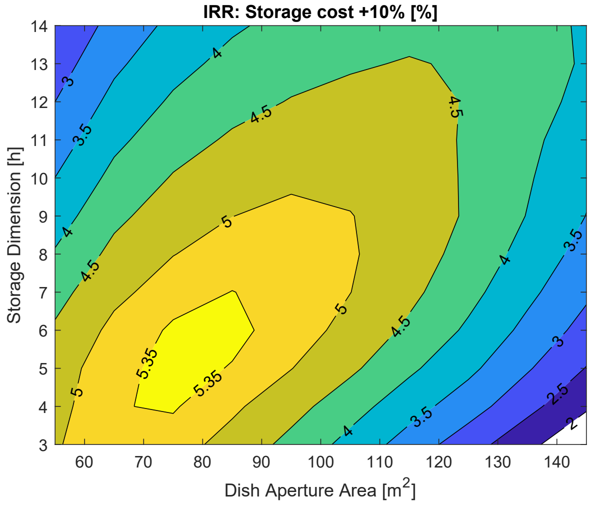


Figure 64: IRR: Increase in Storage Cost of 10%

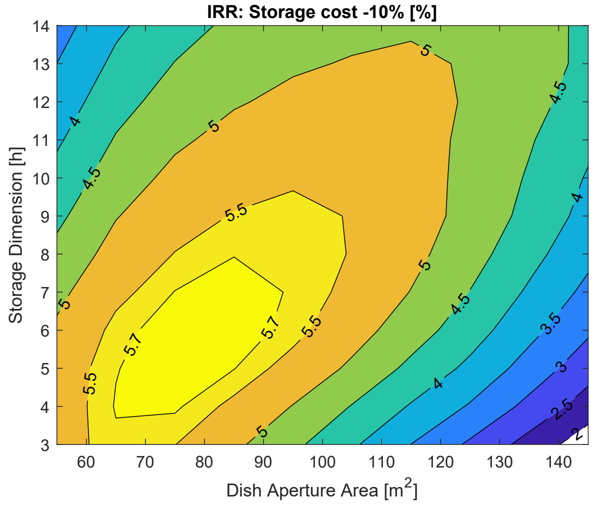


Figure 65: IRR: Decrease in Storage Cost of 10%

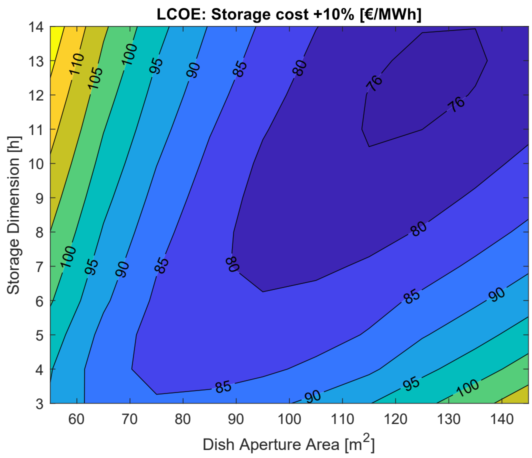


Figure 66: LCOE: Increase in Storage Cost of 10%

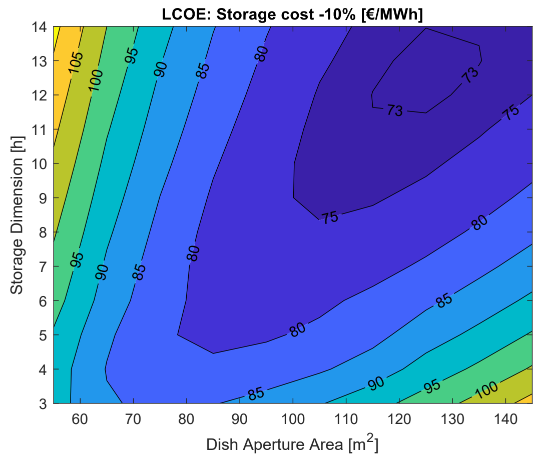


Figure 67: LCOE: Decrease in Storage Cost of 10%

An increase in the storage cost leads to a decrease in the IRR and an increase in th LCOE, as expected. Its variation doesn't affect significantly the optimal configuration of the system, that is always around a storage size of 5 hours and a dish aperture area of 75 $m^2$ (accordingly to the IRR).

A variation of the storage cost by +25% would lead to a slight shift in the optimal configuration for higher storage sizes ( 6 hours of storage and 75 $m^2$), with a reduction of the maximum value of the IRR.

## 7.3 Sensitivity analysis: Mirrors Cost

The effect of a variation in the mirror cost has been studied varying is value by +25% and -25%.

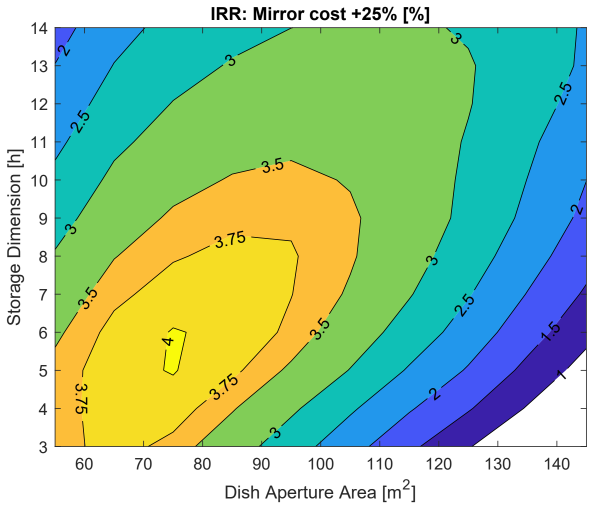


Figure 68: IRR: Increase in Mirrors Cost of 25%

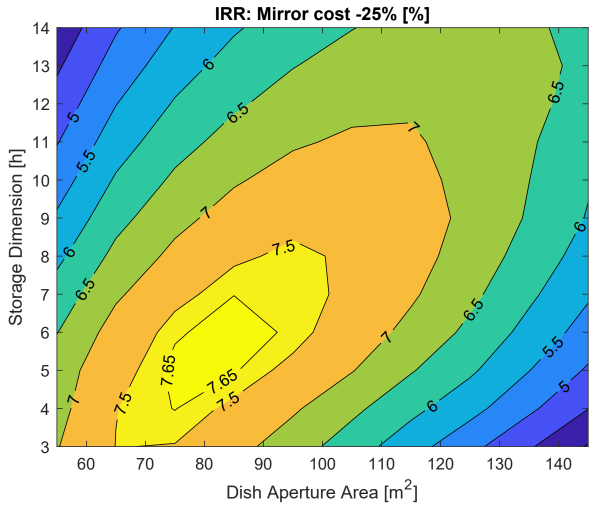


Figure 69: IRR: Decrease in Mirrors Cost of 25%

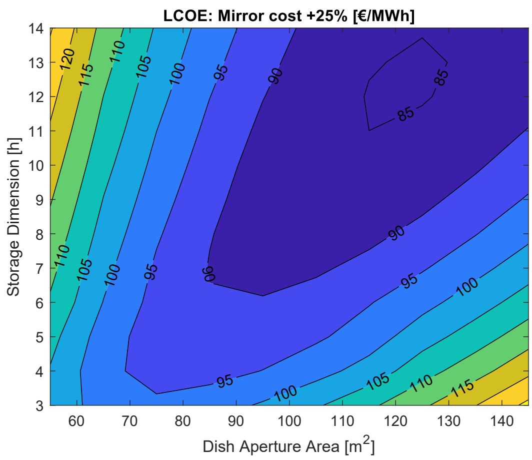


Figure 70: LCOE: Increase in Mirrors Cost of 25%

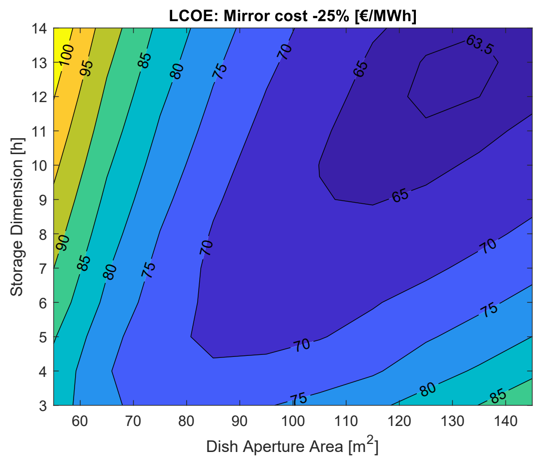


Figure 71: LCOE: Decrease in Mirrors Cost of 25%

The variation of the mirror cost affects significantly the value of the LCOE and the IRR. An increase in the mirror costs shift the optimal configuration of the system for higher mirror areas values and higher storage sizes. Increasing its cost by +25% would shift the optimal configuration of the system for a mirror area around $85m^2$ and a 6 hours storage size. A decrease in the mirrors cost could really increase the competitiveness of the solar dish.

## 7.4 Sensitivity analysis: Incentives

The application of incentives in the case study has a non-neglegible effect into the optimal performance of the plant and in the numerical value of the IRR.

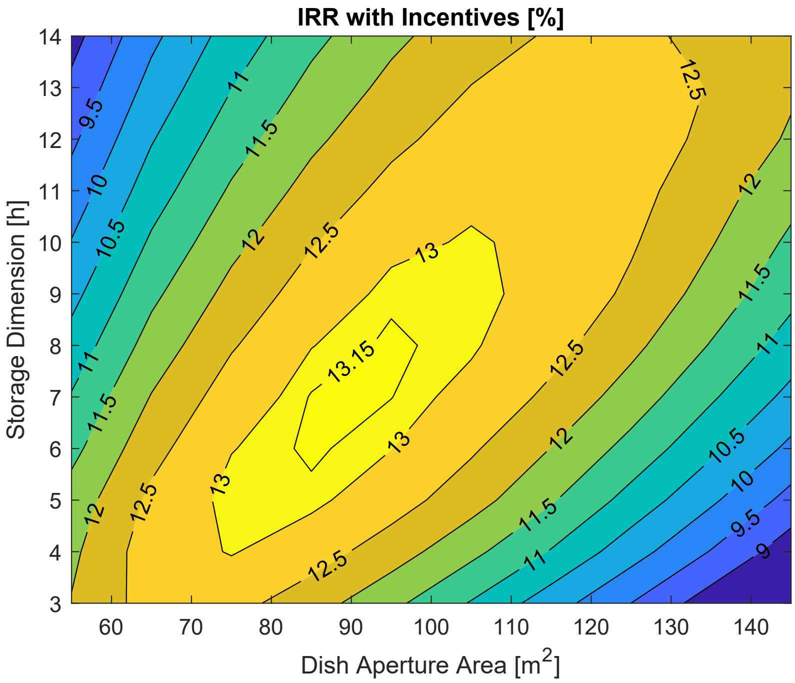


Figure 72: IRR with incentives

As it can be observed in figure 72, the application of incentives shift the optimal configuration for higher value of storage size and mirror area. This results lead to a optimum that is in between the optimum calculated for the IRR and the LCOE for the main study.
This is due to the fact that the incentives are considered for kWh of energy produced. This means that the quantity of energy generated will play a much more important role with respect to the previous cases.

## 7.5 Sensitivity analysis: Location Selection

In order to study the effect that a different location selection could have on the economical performance of the power-plant, the new location Sydney has been considered. This location is characterized by a much lower DNI value with respect to Woomera. Its value is lower than 1900kWh/$m^2$.

This low DNI variation causes a shift of the optimal performance of the plant for higher values of mirrors area and causes also a significant variation of the IRR and LCOE values, as expected (figure 73).

The shifting was expected as long as, in order to obtain a significant amount of energy for the system that could cover the total expenditure for the solar dish, a higher productivity of the power plant is needed.

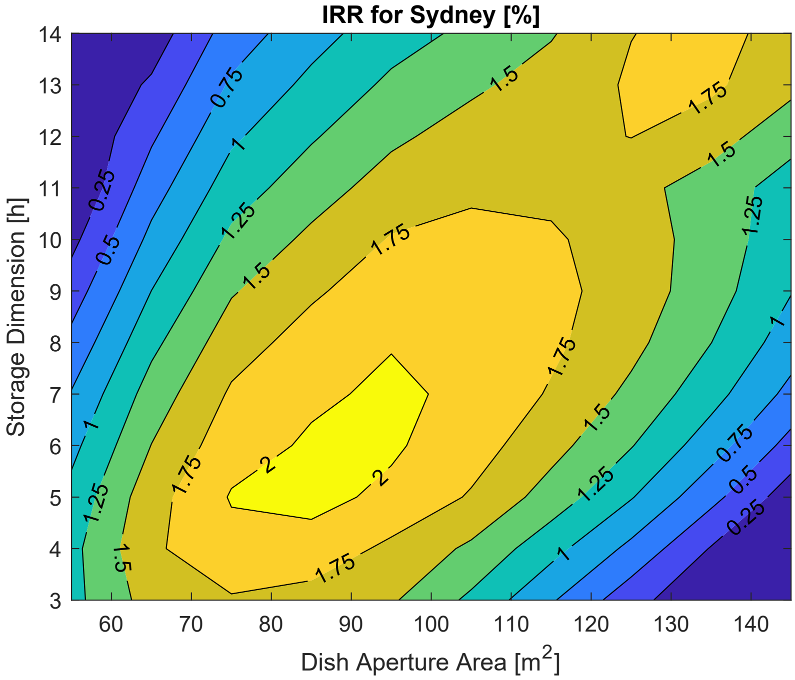


Figure 73: IRR for Sydney

A similar effect can be observed in the LCOE plot (74). Its value is also much higher with respect to the one calculated for Woomera.

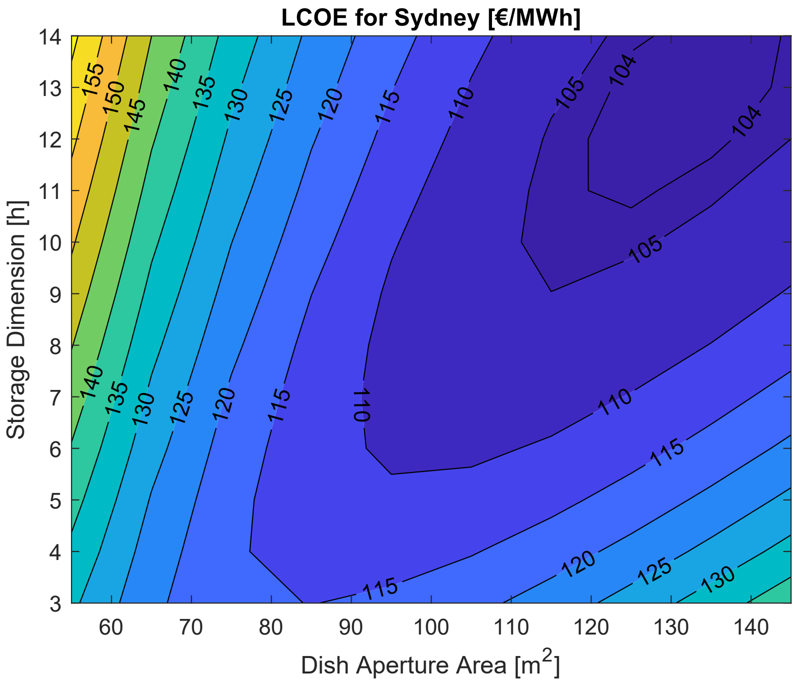


Figure 74: LCOE for Sydney

# 8 Conclusions

In this study, the possibility of using a storage system incorporated into a solar dish stirling system has been studied through a pre-feasibility study of the plant.

Two different storage models have been developed: a simplified 0D model and a more complex 1D Finite difference model. The effect of the variation of the storage aspect ratio has been evaluated in both of them, showing the beneficial effect that an increase of that parameter could create.

A control strategy has been developed to regulate the on-off state of the system to maximize the profit obtainable for the dish.

The control strategy and the first 0D model have been coupled with the a simplified solar dish model to perform the pre-feasibility study of the system for the South Australian market. After an analysis of the possible locations, Woomera has been chosen because of its high DNI value and the proximity to a substation of the national electric grid.

The results have shown that the system is characterized by relatively low value of the LCOE and acceptable values for the IRR (LCOE of 74 €/MWh and IRR of 5.5%). Those values have demonstrated a high dependency on the variation of both the storage and the mirror costs with a slight variation in the optimal configuration for the different cases. A decrease in the mirror cost is fundamental to make the plant more competitive.

The presence of national incentives has shown a high impact on the performance indicator, causing also a non-negligible variation in the most advantageous layout of the solar dish Stirling (higher mirror areas and storage size would be preferred).

The location variation has also shown a very high impact on the economical performance indicators. In fact, very low value of the Internal Rate of Return caused by a decrease in the location DNI would compromise the economical feasibility of the system.

The developed control strategy has demonstrated high economical effectiveness, because of its capability of taking advantage of the high price peaks present in the tariff scheme.

The results are very sensible to variation in the receiver and the solar field efficiency. If the same storage has to be used in different CSP systems (e.g. Solar Tower) a non-constant field efficiency would be needed.

The application of a different tariff scheme would lead to a variation in the IRR results. If a tariff scheme with lower peaks had been considered, the optimal layout of the plant would have been in between the one obtained for the IRR and the one obtained considering the LCOE.

# 9 Model Limitations and Suggestions for Future Work

The described model and analysis could be further refined considering the aspects described below.

- The developed model gives an idea of the functioning of the storage. A much more precise model could be obtained correcting the model accordingly to the results of the CFD simulations (deviation in the heat transfer area due to convection effects in the liquid layer, correction of the Nusselt correlation for the specified case);
- A proper heat transfer system model should be coupled with the storage in order to take into account the temperature differences read into the system;
- A more complex receiver model should be interfaced with the storage model to better understand the effect of a modification of the aspect ratio of the PCM block.
- A deeper analysis on the storage cost should be carried out accordingly to the actual materials and systems used in the real case.

# Bibliography

[1] a. Kribus, H. Ries & W. Spirkl. Inherent Limitations of Volumetric Solar Receivers, 1996.

[2] A. Kribus, P. Doron, R. Rubin, R. Reuven, E. Taragan, S. Duchan & J. Karni. Performance of the Directly-Irradiated Annular Pressurized Receiver (DIAPR) Operating at 20 Bar and 1,200°C, 2000.

[3] Ambra Giovannelli, Muhammad Anser Bashir & Erika Maria Archilei. High-Temperature Solar Receiver Integrated with a Short-Term Storage System, 2017.

[4] Antonio L.Ávila-Marín. Volumetric receivers in Solar Thermal Power Plants with Central Receiver System technology: A review, 2011.

[5] Australian Government: Clean Energy Regulator. Large-scale Renewable Energy Target. `http://www.cleanenergyregulator.gov.au/RET/About-the-Renewable-Energy-Target/How-the-scheme-works/Large-scale-Renewable-Energy-Target`, 2017.

[6] B. Nedjar. An enthalpy-based finite element method for nonlinear heat problems involving phase change, 2002.

[7] Brian D. Iverson & Clifford K. Ho. Review of High-Temperature Central Receiver Designs for Concentrating Solar Power, 2014.

[8] C. E. Andraka. Dish Stirling advanced latent storage feasibility, 2013.

[9] Charles E. Andraka. Solar Heat-Pipe Receiver Wick Modeling. `https://www.osti.gov/scitech/servlets/purl/2816`, 1999.

[10] Charles E. Andraka, K. Scott Rawlinson & Nate P. Siegel. Technical Feasibility of Storage on Large Dish Stirling Systems, 2012.

[11] CSP Library. CSP Library. `http://cspworld.org/resources/what-csp`. Accessed: 2017-09-08.

[12] Desertec-UK. CSP Pictures. `http://www.trec-uk.org.uk/resources/pictures/stills3.html`, 2009.

[13] Edward L. Hoffman, Charles M. Stone. Structural Analysis of a Reflux Pool-Boiler Solar Receiver. `https://www.osti.gov/scitech/servlets/purl/5168668`, 1991.

[14] Electranet. Network Map. https://www.electranet.com.au/what-we-do/solutions/network-map/, .

[15] EnergyPlus. Weather Data. https://energyplus.net/weather, .

[16] Feng Li, Yongjun Hu, Renyuan Zhang. The Influence of Heating-Cooling Cycles on the Thermal Storage Performances of Al-17 Wt.% Si Alloy, 2011.

[17] Gaosheng Wei, Pingrui Huang, Chao Xu, Dongyu Liu, Xing Ju, Xiaoze Du, Lijing Xing, Yongping Yang. Thermophysical property measurements and thermal energy storage capacity analysis of aluminum alloys, 2016.

[18] Giacomo Gavagnin, David Sánchez, Gonzalo S. Martínez, José M. Rodríguez, Antonio Muñoz. Cost analysis of solar thermal power generators based on parabolic dish and micro gas turbine: Manufacturing, transportation and installation, 2017.

[19] Gianmarco Ragnolo. A techno-economic comparison of a Micro Gas-Turbine and a Stirling Engine for Solar Dish application, 2014.

[20] Helioscsp. Concentrated Solar Power installed capacity increased to 4940 MW by the end of 2015. http://helioscsp.com/concentrated-solar-power-installed-capacity-increased-to-4940-mw-by-the-end-of-2015/, 2016.

[21] IRENA. Concentrating Solar Power, 2012.

[22] Johannes P. Kotzè, Theodor W. von Backstrom, Paul J. Erens. High Temperature Thermal Energy Storage Utilizing Metallic Phase Change Materials and Metallic Heat Transfer Fluids. http://solarenergyengineering.asmedigitalcollection.asme.org/article.aspx?articleid=1692818, 2013.

[23] John A. Duffie & William A. Beckman. Solar Engineering of Thermal Processes, Fourth Edition. https://www.advan-kt.com/solarengineering.pdf, 2013.

[24] Julianna Schmitz, Bengt Hallstedt, Ju¨rgen Brillo, Ivan Egry, Michael Schick. Density and thermal expansion of liquid Al–Si alloys, 2011.

[25] Keith Lovegrove & Wes Stein. Concentrating solar power technology: Principles, developments and applications, 2012.

[26] Luisa F. Cabeza, Aran Solé, Xavier Fontanet, Camila Barreneche, Aleix Jové, Manuel Gallas, Cristina Prieto, A. Inés Fernández. Thermochemical energy storage by consecutive reactions for higher efficient concentrated solar power plants (CSP): Proof of concept, 2017.

[27] M. J. Assael, E. K. Mihailidou, J. Brillo, S.V. Stankus, J.T. Wu, W.A. Wakeham. Reference Correlation for the Density and Viscosity of Eutectic Liquid Alloys Al+Si, Pb+Bi, and Pb+Sn, 2012.

[28] Marc Perez & Richard Perez. A FUNDAMENTAL LOOK AT SUPPLY SIDE ENERGY RESERVES FOR THE PLANET. http://asrc.albany.edu/people/faculty/perez/2015/IEA.pdf, 2015.

[29] Meriem Chaanaoui, Sébastien Vaudreuil & Tijani Bounahmidi. Benchmark of Concentrating Solar Power Plants: Historical, Current and Future Technical and Economic Development. http://www.sciencedirect.com/science/article/pii/S1877050916302009, 2016.

[30] Mihajlo Firak. Comparative analysis of the solar dish electricity production, 2005.

[31] Mohamad Muhieddine, Edouard Canot, Ramiro March. Various Approaches for Solving Problems in Heat Conduction with Phase Change, 2009.

[32] Mohammad H. Ahmadia, Mohammad-Ali Ahmadib, Fathollah Pourfayaza. Thermal models for analysis of performance of Stirling engine: A review, 2017.

[33] N. Hannoun, V. Alexiades, T. Z. Mai. A reference solution for phase change with convection, 2005.

[34] nrc. Capacity factor (net). https://www.nrc.gov/reading-rm/basic-ref/glossary/capacity-factor-net.html. Accessed: 2017-09-08.

[35] Octobre J. & Guihard F. Systèmes Solaires, 2009.

[36] PSA. Dish Stirling Systems - DISTAL I. https://www.psa.es/en/instalaciones/discos/distal1.php, .

[37] Rafael E. Guédez. Lecture presentation: Design of Solar Tower CSP plants , 2017.

[38] Robert Sier. Solar Stirling Engines. http://www.stirlingengines.org.uk, 2017.

[39] Roberta Mancini. Volumetric Solar Receiver for a Parabolic Dish and Micro-Gas Turbine system, 2015.

[40] Ruel A Overfelt, Sayavur I Bakhtiyarov, Raymond E Taylor. Thermophysical properties of A201, A319, and A356 aluminium casting alloys, 2002.

[41] Ryo Fukahori, Takahiro Nomura, Chunyu Zhu, Nan Sheng, Noriyuki Okinaka, Tomohiro Akiyama. Thermal analysis of Al–Si alloys as high-temperature phase-change material and their corrosion properties with ceramic materials, 2015.

[42] S. I. Bakhtiyarov, R. A. Overfelt, S. G. Teodorescu. Electrical and thermal conductivity of A319 and A356 aluminum alloys, 2001.

[43] Saleh Nasser AL-Saadi, Zhiqiang (John) Zhai. Modeling phase change materials embedded in building enclosure: A review, 2013.

[44] Sarada Kuravi, D. Yogi Goswami, Elias K. Stefanakos, Manoj Ram, Chand Jotshi, Swetha Pendyala, Jamie Trahan, Prashanth Sridharan, Muhammad Rahman & Burton Krakow. THERMAL ENERGY STORAGE FOR CONCENTRATING SOLAR POWER PLANTS, 2013.

[45] Sean Farrell. Jimmy Carter leases his land to solar power much of Plains. http://unitedsolarinitiative.org/category/news/, 2016.

[46] Solargis. Solar resource maps and GIS data for 200+ countries. https://solargis.com/products/maps-and-gis-data/overview/, 2018.

[47] Thomas Fend & Louy Qoaider. enerMENA CSP Teaching Materials, .

[48] William B. Stine & Richard B. Diver. A compendium of Solar Dish/Stirling Technology, 1994.

[49] World Energy Council. World Energy Resources 2016. https://www.worldenergy.org/wp-content/uploads/2016/10/World-Energy-Resources_SummaryReport_2016.10.03.pdf, 2016.

[50] Yosr Allouche. PCM ENERGY STORAGE MODELING: CASE STUDY FOR A SOLAR-EJECTOR COOLING CYCLE, 2016.

[51] Yvan Dutil, Daniel R. Rousse, Nizar Ben Salah, Stephane Lassue, Laurent Zalewski. A review on phase-change materials: Mathematical modeling and simulations, 2011.

[52] Zhengyun Wang, Hui Wang, Xiaobo Li, Dezhi Wang, Qinyong Zhang, Gang Chen c, Zhifeng Ren. Aluminum and silicon based phase change materials for high capacity thermal energy storage, 2015.

[53] Zhengyun Wang, Hui Wang, Xiaobo Li, Dezhi Wang, Qinyong Zhang, Gang Chen, Zhifeng Ren. Aluminum and silicon based phase change materials for high capacity thermal energy storage, 2015.

# Appendix A: Mirror cost function

The cost of the mirror is evaluated accordingly to the following equations:

$$C_{Man,Dish} = c_{Man,Dish} * f_{N,Dish} * A_{Dish} \tag{47}$$

$$c_{Man,Dish} = a_{A,Dish} * A_{Dish}^2 + b_{A,Dish} * A_{Dish} + c_{A,Dish} \tag{48}$$

$$f_{N,Dish} = a_{N,Dish} * L_{Dish}^{b_{N},Dish} + c_{N,Dish} \tag{49}$$

where:

- $C_{Man,Dish}$: total manufacturing cost of the solar dish [€] ;
- $c_{Man,Dish}$: Specific manufacturing cost of the solar dish per unit aperture area [€/$m^2$];
- $f_{N,Dish}$: correction factor for production rate;
- $A_{Dish}$: Dish aperture area[$m^2$];
- $L_{Dish}$:annual production rate [units/year] set to 1000 units/year;
- $a_{A,Dish}, b_{A,Dish}, c_{A,Dish}, a_{N,Dish}, b_{N,Dish}, c_{N,Dish}$: coefficients presented in the table below.

| Coefficients | a | b | c |
|---|---|---|---|
| $x_{A,Dish}$ | $4.760 * 10^{-3}$ | -0.9140 | 304.54 |
| $x_{N,Dish}$ | 3.610 | -0.3095 | 0.5308 |